Mars Science Laboratory Heatshield Aerothermodynamics: Design and Reconstruction

Karl T. Edquist * Brian R. Hollis †
Christopher O. Johnston ‡
NASA Langley Research Center, Hampton, Virginia 23681

Deepak Bose §
NASA Ames Research Center, Moffett Field, California 94035

Todd R. White ¶
ERC Inc., Moffett Field, California 94035

Milad Mahzari ‖
Georgia Institute of Technology, Atlanta, Georgia 30332

The Mars Science Laboratory heatshield was designed to withstand a fully turbulent heat pulse based on test results and computational analysis on a pre-flight design trajectory. Instrumentation on the flight heatshield measured in-depth temperatures in the thermal protection system. The data indicate that boundary layer transition occurred at 5 of 7 thermocouple locations prior to peak heating. Data oscillations at 3 pressure measurement locations may also indicate transition. This paper presents the heatshield temperature and pressure data, possible explanations for the timing of boundary layer transition, and a qualitative comparison of reconstructed and computational heating on the as-flown trajectory. Boundary layer Reynolds numbers that are typically used to predict transition are compared to observed transition at various heatshield locations. A uniform smooth-wall transition Reynolds number does not explain the timing of boundary layer transition observed during flight. A roughness-based Reynolds number supports the possibility of transition due to discrete or distributed roughness elements on the heatshield. However, the distributed roughness height would have needed to be larger than the pre-flight assumption. The instrumentation confirmed the predicted location of maximum turbulent heat flux near the leeside shoulder. The reconstructed heat flux at that location is bounded by smooth-wall turbulent calculations on the reconstructed trajectory, indicating that augmentation due to surface roughness probably did not occur. Turbulent heating on the downstream side of the heatshield nose exceeded smooth-wall computations, indicating that roughness may have augmented heating. The stagnation region also experienced heating that exceeded computational levels, but shock layer radiation does not fully explain the differences.

*Aerospace Engineer, Atmospheric Flight and Entry Systems Branch, Mail Stop 489, AIAA Senior Member, karl.t.edquist@nasa.gov.
†Aerospace Engineer, Aerothermodynamics Branch, AIAA Associate Fellow.
‡Aerospace Engineer, Aerothermodynamics Branch, AIAA Member.
§Senior Research Scientist, Aerothermodynamics Branch, AIAA Associate Fellow.
¶Research Scientist, Aerothermodynamics Branch, AIAA Member.
‖Graduate Research Assistant, Guggenheim School of Aerospace Engineering, AIAA Student Member.

Nomenclature

A	reference area, $\frac{1}{4}\pi D^2$ (m^2)
C_D	drag coefficient, $D/q_\infty A$
C_H	heat transfer coefficient, $q_w/\rho_e V_e(H_e - H_w)$ (m^2/s)
D	aeroshell diameter (m)
D_{im}	multi-component diffusion coefficient (m^2/s)
H	total enthalpy (J/kg)
h	altitude (km)
h_i	species enthalpy (J/kg)
k	roughness height (m)
k^+	roughness augmentation Reynolds number, $\rho_w U_\tau k_s/\mu_w$
k_s	equivalent sand-grain roughness height (m)
M	Mach number
m	entry system mass (kg)
p	pressure (Earth atm, 1 Earth atm = 101,325 Pa)
Q	convective heat load, $\int q\,dt$ (J/cm^2)
q	heating rate (W/cm^2)
q_∞	freestream dynamic pressure, $\frac{1}{2}\rho_\infty V_\infty^2$ (Pa)
Re_∞	freestream Reynolds number, $\rho_\infty V_\infty D/\mu_\infty$
$Re_{k,k}$	roughness Reynolds number, $\rho_k u_k k/\mu_k$
Re_θ	momentum thickness Reynolds number, $\rho_e u_e \theta/\mu_e$
St	Stanton number, $q_w/\rho_\infty V_\infty(H_\infty - H_w)$
T	temperature (^oC)
t	time from atmospheric interface (s)
U_τ	shear velocity, $\sqrt{\tau_w/\rho_w}$ (m/s)
V	velocity relative to atmosphere (km/s)
α	angle of attack (deg)
γ	inertial flight path angle (deg)
ϵ	emissivity
θ	momentum thickness (m)
ρ	density (kg/m^3)
σ	Stefans constant = 5.67 x 10^{-8} $W/(m^2 - K^4)$
τ	shear stress (Pa)

Acronyms

AEDC	Arnold Engineering Development Center
B-L	Baldwin-Lomax
BET	best estimated trajectory
BLT	boundary layer transition
CEV	Crew Exploration Vehicle
CFD	computational fluid dynamics
CUBRC	Calspan University of Buffalo Research Center
DPLR	Data Parallel Line Relaxation
EDL	entry, descent, and landing
FIAT	Fully-Implicit Ablation and Thermal response code
HARA	Hypersonic Air Radiation Algorithm
LAURA	Langley Aerothermodynamic Upwind Relaxation Algorithm
MEADS	MEDLI Entry Air Data System
MEDLI	MSL Entry, Descent, and Landing Instrumentation
MISP	MEDLI Integrated Sensor Plugs
MSL	Mars Science Laboratory
PICA	Phenolic Impregnated Carbon Ablator
SCLK	spacecraft clock time
SLA	Super Lightweight Ablator
SST	Shear Stress Transport
TC	thermocouple
TPS	thermal protection system

Subscripts

D	aeroshell diameter
e	boundary layer edge ($H_e = 0.995 H_\infty$)
i	atmospheric interface
r	recovery
lam	laminar
$turb$	turbulent
w	wall
$w, 0$	smooth wall
w, k	rough wall
∞	freestream

I. Introduction

The Mars Science Laboratory (MSL) entry, descent, and landing (EDL) system[1] successfully delivered the 900-kg *Curiosity* rover to the surface of Mars on August 5^{th}, 2012. The EDL system (Figure 1) consisted of a rigid aeroshell (4.5 meters) and a supersonic parachute (21.5 meters), both of which were similar to, but larger than, previous Mars EDL systems. The Viking[2] landers used 3.5-m heatshields, whereas Pathfinder,[3] the Mars Exploration Rovers,[4] and Mars Phoenix[5] each used a 2.65-m heatshield. MSL's powered descent system used the the Sky Crane maneuver to deliver the rover to a soft touchdown less than 2 kilometers from the landing target in Gale crater. Prior to parachute deployment, the MSL aeroshell was designed to fly with a hypersonic lift-to-drag ratio of 0.24 at an angle of attack (α) magnitude near 16 degrees using an Apollo-derived guidance algorithm and reaction control jets to control the lift vector direction (Figure 2).

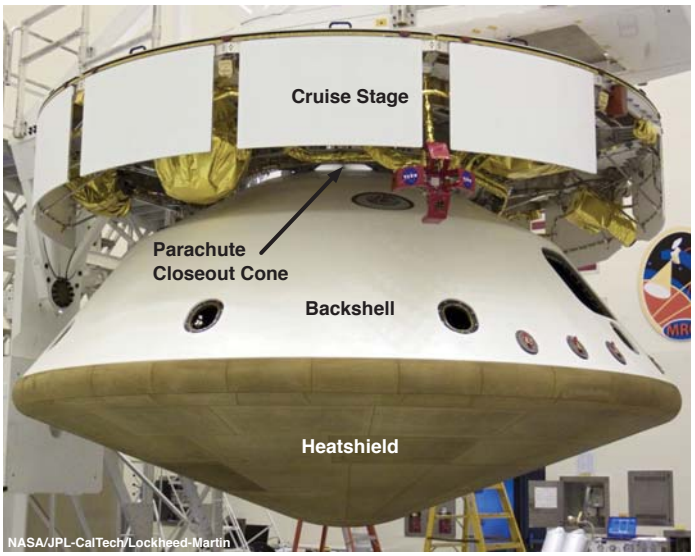

Figure 1. Spacecraft Assembly with 4.5-m Heatshield

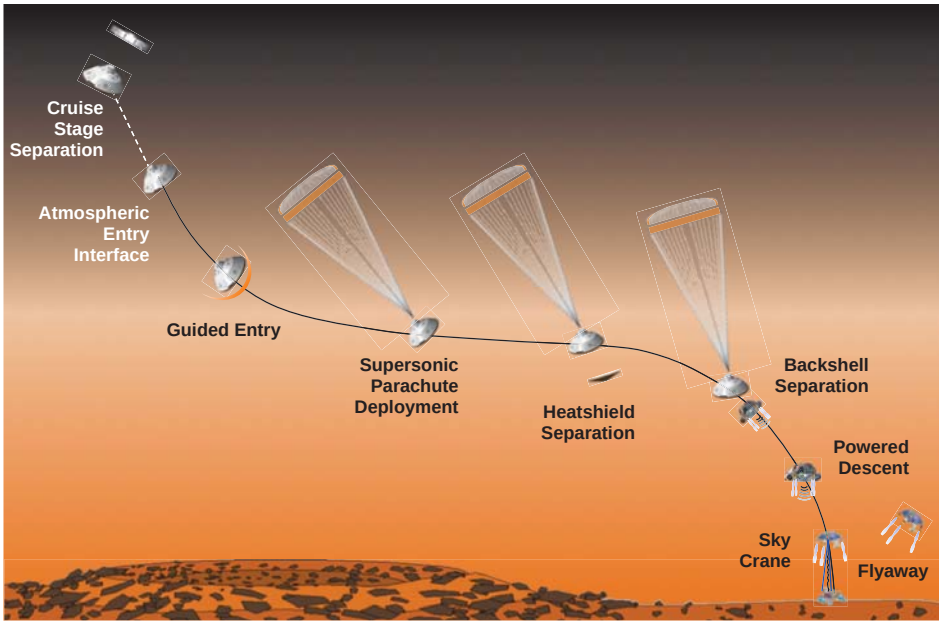

Figure 2. Entry, Descent, and Landing Sequence

Pre-flight analysis and ground testing concluded that the unprecedented size (4.5-m heatshield) and mass (3153 kg at atmospheric entry) of the MSL entry system would lead to boundary layer transition (BLT) on the heatshield prior to the time of peak heating.[6−7] Computational models predicted that turbulence would cause the maximum convective heat flux to occur at locations away from the heatshield's nose. None of the previous Mars lander missions, which had smaller heatshields (less than 3.5 meters) and lower ballistic coefficients (m/C_DA, less than 90 kg/m^2) compared to MSL, were not predicted to encounter BLT until after peak heating, if at all. Previous capsules used the Super-Lightweight Ablator (SLA-561V) heatshield thermal protection system (TPS) that was sized for laminar conditions on the nose at peak heating. However, no instrumentation was successfully implemented on any SLA heatshield to measure turbulent conditions away from the nose, if they occurred. Temperature measurements on the Mars Pathfinder heatshield[8] did not provide conclusive results on boundary layer transition near the shoulder.

The prediction of BLT led to two changes in the MSL heatshield design.[9] First, turbulent conditions on the heatshield flank resulted in heating rates that exceeded those on the nose. High heat flux away from the stagnation point led to new test procedures on wedge specimens that eventually uncovered SLA-561V failures.[10] The MSL project switched to the Phenolic Impregnated Carbon Ablator (PICA)[11] material for the heatshield due to its demonstrated success on the Stardust sample return capsule[12] and ongoing development within the Orion Crew Exploration Vehicle (CEV) program.[13] A uniform heatshield thickness was specified within mass constraints rather than the usual method of sizing the TPS to surface heating conditions; this strategy was chosen due to the late change in heatshield material. Thermal analysis showed that the flight heatshield was thicker than necessary to maintain a TPS/structure interface temperature below 250^oC.[9]

The prediction of turbulent conditions at peak heating also contributed to the addition of the MSL EDL Instrumentation[14] (MEDLI) package. Figure 3 shows the MEDLI sensor layout on the heatshield. The MEDLI Integrated Sensor Plugs (MISP) consisted primarily of in-depth thermocouples (TCs) at seven heatshield locations. The MISP system was designed to measure in-depth TPS temperatures to permit detection of BLT and allow post-flight reconstruction of surface heat flux. Sensors T2 and T3 on the heatshield's leeside ($X < 0$) were expected to take measurements near the maximum turbulent heat flux location. The MEDLI Entry Air Data System (MEADS) measured surface pressure at seven separate heatshield locations through 0.1-inch holes drilled into the heatshield. The MEADS pressure ports were arranged in a cruciform pattern to reconstruct the dynamic pressure and the entry capsule's wind-relative attitude (angles of attack and sideslip) more accurately than is possible with conventional inertial measurements.

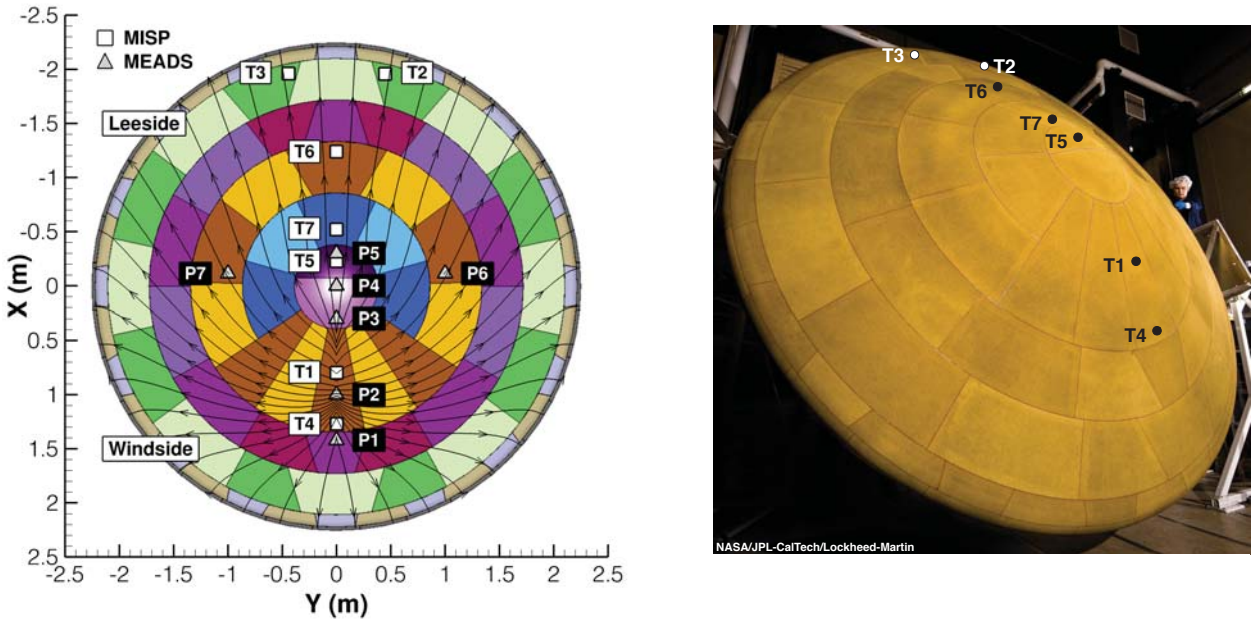

(a) MEDLI Sensor Locations with Predicted Streamlines at Peak Heating on the BET

(b) PICA TPS (113 Tiles) and MISP Locations

Figure 3. Heatshield and MEDLI Sensor Locations

The MSL project conducted tests in multiple facilities to better understand heatshield BLT and turbulent heating. These tests were designed to observe smooth-wall BLT and correlate the onset of transition to parameters that could be predicted at Mars flight conditions. The turbulent data also provided on opportunity to assess the accuracy of computational turbulence models that had not been needed previously for any Mars mission. Numerous computational[15−21] and experimental[22−27] studies have been written that summarize the analyses for various MSL aeroshell configurations and design trajectories. Recent studies[28−37] have used the MISP and MEADS data to reconstruct the as-flown aerodynamics and aerothermodynamics. This paper continues the post-flight analysis by focusing on the MISP temperature data and updated computational fluid dynamics (CFD) analysis on the BET. The following specific topics will be covered:

- Review of pre-flight testing and analysis of smooth-wall BLT and turbulent heating
- Review of pre-flight aerothermodynamic environments for heatshield TPS design
- Quantitative comparison of reconstructed surface pressure to CFD results on the BET
- Observations of BLT in the MISP temperature data
- Qualitative comparison of reconstructed heat flux to CFD results on the BET
- Analysis of surface roughness effects on convective heating
- Initial assessment of heating from shock layer radiation

II. Review of Pre-Flight Testing and Analysis

The process for defining aerothermodynamic environments (surface heat flux, pressure, and shear stress versus time) to support TPS testing, modeling, and design was previously described[6] for the original 2009 launch date (2010 landing). Updates to the environments for the re-scheduled 2011 launch date (2012 landing) were also generated using the same process and updated design trajectories.[7] Flight environments were based on CFD predictions using the Langley Aerothermodynamic Upwind Relaxation Algorithm (LAURA)[38] code and supporting calculations from the Data Parallel Line Relaxation (DPLR)[39] code. The same process that was used to define aerothermal environments for TPS sizing was also used to define environments at each MISP location on the pre-flight TPS design trajectory. The following sections revisit the pre-flight testing and computational analyses that supported the expectation of turbulent conditions at peak heating.

A. Boundary Layer Transition and Turbulent Heating

The decision to design the MSL heatshield for turbulent conditions was initially based on pre-flight CFD solutions that showed a high likelihood of smooth-wall BLT for various design trajectories. None of the Mars lander missions prior to MSL had any expectation of turbulent conditions prior to peak heating, so available ground test data were minimal. Subsequent testing by the MSL project in perfect gas and high-enthalpy hypersonic facilities provided smooth-wall laminar and turbulent heating data over a range of Reynolds numbers.[22−24] Table 1 summarizes the aeroheating tests conducted by the MSL project specifically to examine BLT and turbulent heating on sub-scale models. The Arnold Engineering Development Center (AEDC) Tunnel 9 (nitrogen) and the NASA Langley Research Center 20-Inch Mach 6 Tunnel (air) were the primary perfect gas facilities used to examine BLT and turbulent heating. High-enthalpy testing in CO_2 was also conducted in the California Polytechnic University (CalTech) T5 Hypervelocity Shock Tunnel[24] and the Calspan-University of Buffalo Research Center (CUBRC) Large Energy National Shock Tunnel (LENS).

Table 1. Summary of BLT and Turbulent Heating Ground Tests[22−24]

Facility	Gas	D_{model} (in)	M_∞	$Re_\infty/ft \times 10^{-6}$	$H \times 10^{-6}$ (J/kg)
AEDC Tunnel 9	N_2	6	8, 10	1.0 - 49.0	0.5 - 0.8
Langley 20-Inch Mach 6	Air	6, 7, 8	6	2.0 - 7.5	0.2
CalTech T5	CO_2	7	4.5	0.35 - 2.9	2.0 - 15.2
CUBRC LENS I	CO_2	12	6.5	0.14 - 0.64	5.0

The ground test data from the AEDC and Langley tests were used to correlate smooth-wall transition as a function of laminar boundary layer *momentum thickness Reynolds number* (Re_θ). The Re_θ parameter is commonly used as an indication of smooth-wall BLT:

$$Re_\theta = \frac{\rho_e u_e \theta}{\mu_e} \tag{1}$$

where the boundary layer *momentum thickness* (θ) is defined as:

$$\theta = \int_0^e \frac{\rho u}{\rho_e u_e} \left(1 - \frac{u}{u_e}\right) d\eta \tag{2}$$

Figure 4 shows heating data from the AEDC and Langley tunnels. The observed heat flux is normalized by the LAURA laminar heat flux, the result of which was used to indicate the boundary layer conditions (= 1 indicates laminar, > 1 indicates transitional or turbulent). The data were correlated to CFD-based laminar Re_θ to aid in the pre-flight TPS design. Transition was observed to occur on smooth models at Re_θ near 250 in the middle of the data scatter. The slope of the data rises quickly for Re_θ above 300 and follows a relatively constant slope thereafter towards the highest Reynolds numbers, indicating fully turbulent conditions. In order to conservatively account for the myriad of differences between perfect gas test facilities and Mars flight conditions, a transition criterion of $Re_\theta > 200$ was established for heatshield TPS design. Roughness-induced boundary layer transition due to TPS ablation would have only accelerated transition, but no roughness-based BLT criterion was established.

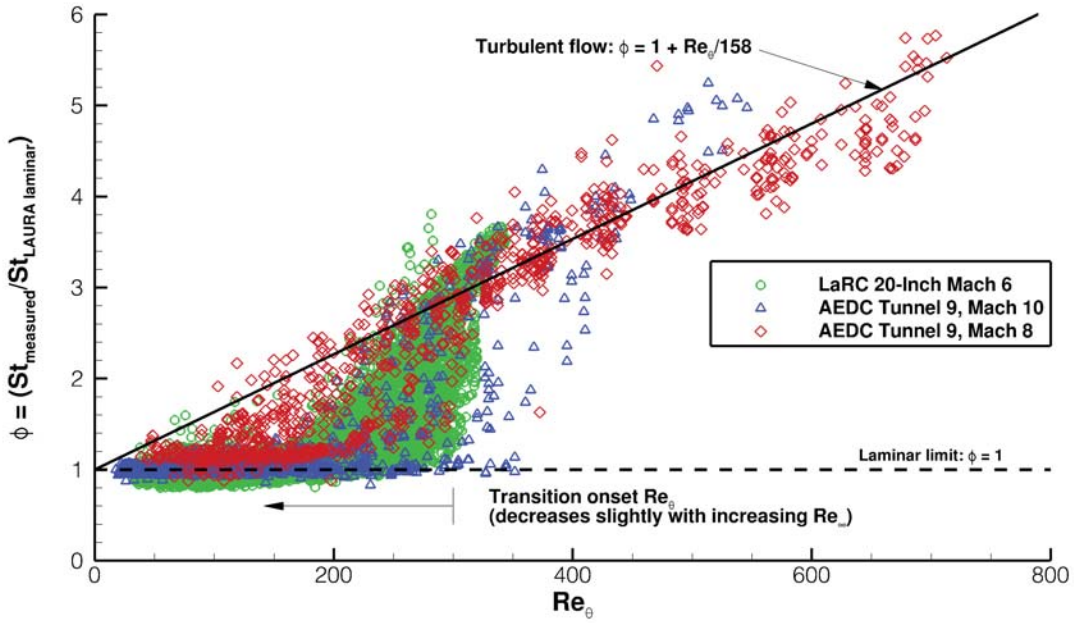

Figure 4. Turbulent-to-Laminar Heating Ratio Correlated to Laminar Re_θ from Perfect Gas Wind Tunnel Data[22]

The AEDC testing also provided data to compare against CFD predictions at laminar and turbulent conditions. Figure 5 shows sample heating results from testing at AEDC. At low Reynolds numbers, laminar conditions existed at all measurement locations on the model forebody (Figure 5a). LAURA and DPLR qualitatively and quantitatively agree with the data; both codes show laminar heat fluxes that are within 12% of the data. At high Reynolds numbers, turbulent conditions existed without the use of boundary layer trips (Figure 5b). The Baldwin-Lomax[40] (B-L) algebraic turbulence model in both LAURA and DPLR compare to the data nearly as well as did the laminar calculations. The main discrepancy between turbulent data and CFD occurred in the stagnation region ($0.6\ in < X < 1.6\ in$) at lower heating levels. In this area, the data shows a bump in heating from an unknown source. This same feature was observed in other test

data;[22] it is believed to be unique to a blunted sphere-cone at a high enough angle of attack such that the stagnation point shifts off the nose and onto the windside conical flank. Tunnel freestream noise also may have contributed to the heating bump. An additional uncertainty was applied to the stagnation point TPS design environments to reflect the uncertainty in the heating augmentation source. The DPLR implementation of the two-equation Shear Stress Transport[41] (SST) model predicted higher turbulent heating on the leeside flank than did the algebraic models. Based on the good agreement between the Baldwin-Lomax model results and perfect gas data, the same turbulence model was also used for predictions at Mars flight conditions.

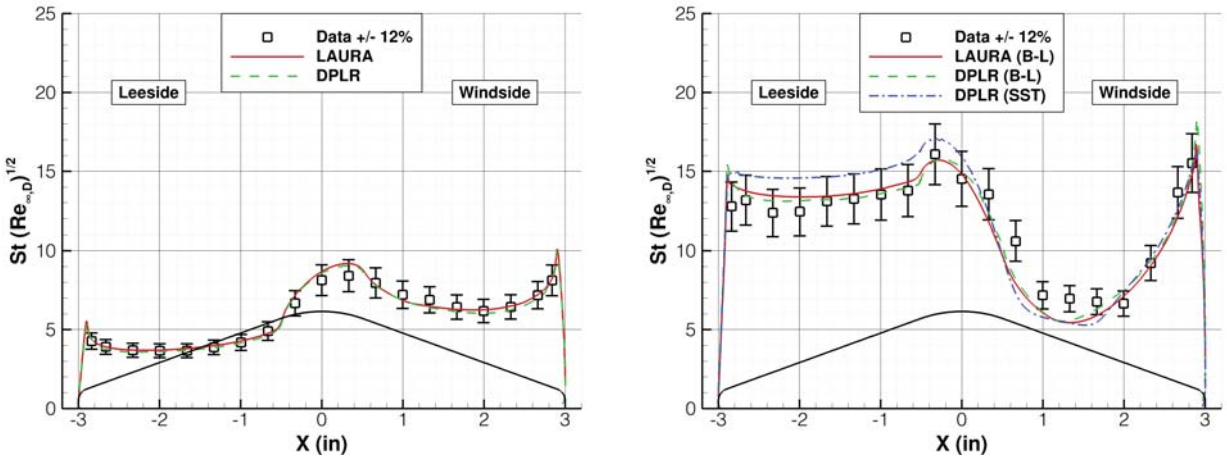

(a) Laminar ($M_\infty = 10, Re_\infty = 1.85 \times 10^6/ft, \alpha = 16\ deg$) (b) Turbulent ($M_\infty = 8, Re_\infty = 30.4 \times 10^6/ft, \alpha = 16\ deg$)

Figure 5. CFD Heating Compared to Data from AEDC Tunnel 9

In addition to the turbulent heating comparisons to AEDC data, comparisons were also performed with the high-enthalpy CO_2 data from the Caltech and CUBRC facilities. While the comparisons were less satisfactory than for the low-enthalpy, perfect gas cases from Langley and AEDC, the measured turbulent heating levels were generally bounded by the computational models employed (i.e. non-catalytic vs super-catalytic) and the differences were incorporated into the overall uncertainty. At the time, the differences between CFD and test data were attributed to uncertainty regarding the surface catalytic efficiency of the wind tunnel model surfaces and to the potential deficiencies in the computational chemical kinetic models. Subsequent analyses[25] have also indicated that the uncertainties in defining the freestream chemical and vibrational excitation of CO_2 for reflected shock tunnels, such as Caltech T5 and CUBRC LENS, have a large effect on the resulting comparisons. Therefore, significant uncertainties remain in the definition of high-enthalpy CO_2 heating environments due to the challenges in obtaining high-fidelity data for validation of computational models.

LAURA laminar solutions were run on the pre-flight TPS design trajectory to estimate smooth-wall BLT at flight conditions. Figure 6 indicates that much of the heatshield leeside ($X < 0$) was predicted to experience laminar Re_θ values well above 200 at the time of peak heating (75.8 seconds). The transition criterion was predicted to be exceeded prior to peak heating at MISP locations T2, T3, T6, and T7. Locations T2 and T3 were expected to experience transition prior to T6 and T7. Neither T1 nor T4 was expected to experience smooth wall transition. Given the uncertainty in predicting transition onset and the effects of TPS surface roughness, which would only accelerate transition, the aerothermal design environments for TPS sizing were developed assuming a fully-turbulent heat pulse over the entire heatshield. Turbulent heating maximizes the integrated heat load and the required PICA thickness in order to remain below the allowable TPS/structure bondline temperature of 250^oC.

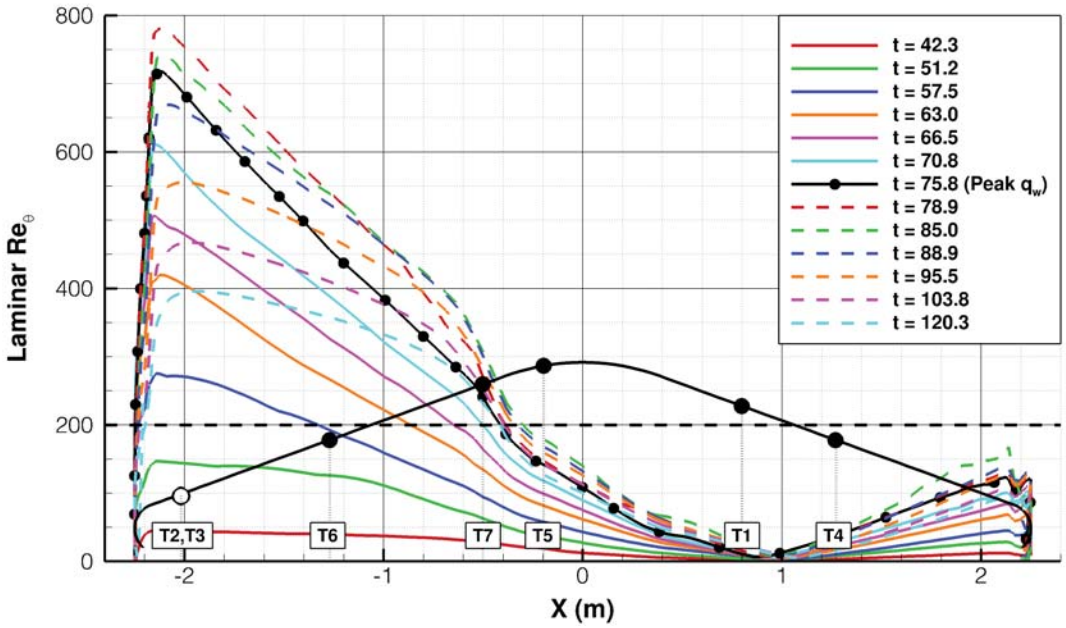

Figure 6. LAURA Laminar Re_θ in the Heathsield Pitch Plane for the Steep TPS Design Trajectory

B. TPS Design Environments

The MSL aerothermodynamic environments were based on LAURA and DPLR Navier-Stokes calculations on the TPS design trajectory. LAURA was also used[42] to predict MSL's aerodynamic characteristics in the hypersonic and supersonic continuum flow regimes, including RCS interference effects. For MSL, turbulent solutions using the Baldwin-Lomax algebraic model were obtained based on the expectation of turbulent transition in flight and the good agreement with perfect gas wind tunnel data. The model assumptions for flight calculations were as follows:

- Turbulent boundary layer: Baldwin-Lomax algebraic model, transition forced at stagnation point
- Chemical non-equilibrium ($CO_2, CO, N_2, O_2, NO, C, N, O$), 0.97 and 0.03 freestream mass fractions for CO_2 and N_2, respectively
- Thermal non-equilibrium (translational and vibrational temperatures)
- Radiative-equilibrium wall: $q_w = \epsilon\sigma T_w^4$, $\epsilon = 0.89$, $\sigma = 5.67$ x 10^{-8} $W/(m^2 - K^4)$
- *Super-catalytic wall*: recombination of CO_2 and N_2 to freestream mass fractions
- Distributed roughness effects added post-CFD
- Turbulent Schmidt number, $Sc_t = 0.7$

Figure 7 shows the ratio of turbulent-to-laminar smooth-wall heat flux from LAURA super-catalytic solutions on the TPS design trajectory. Locations T2 and T3 were expected to see the largest effects from turbulence if BLT occurred prior to peak heating. On the conical flank and nose (T5, T6, T7), turbulence was expected to increase heating by a smaller amount. Neither T1 nor T4 were expected to experience BLT, but uncertainties were included to cover the stagnation heating bump observed in wind tunnel data.

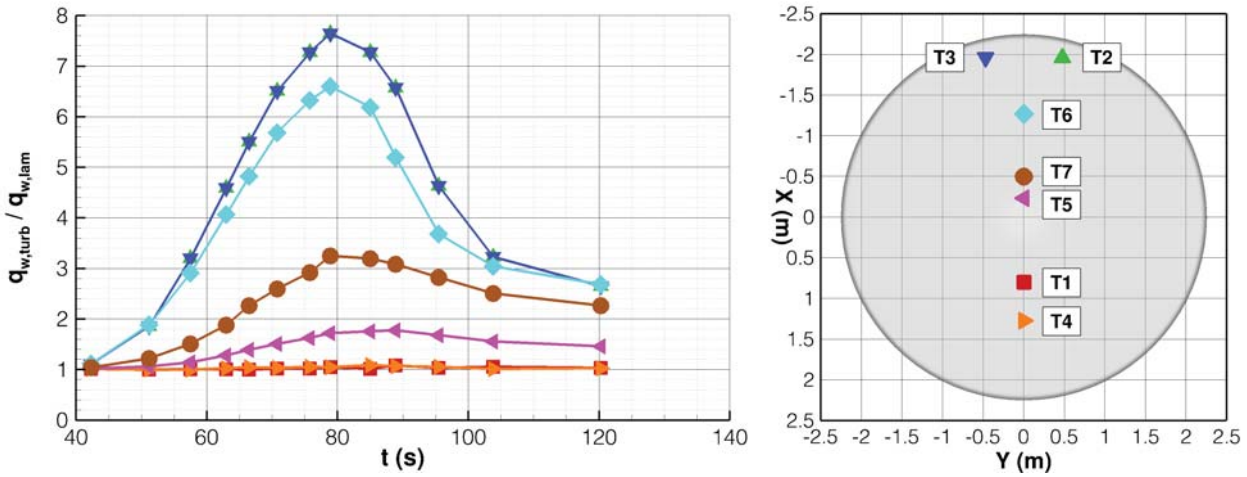

Figure 7. Ratio of LAURA Turbulent-to-Laminar Smooth-Wall Heat Flux (Super-Catalytic) at MISP Locations for the Steep TPS Design Trajectory

The heatshield TPS design environments included uncertainties on the LAURA smooth-wall results to account for un-modeled phenomena and other effects that could worsen the environments.[6] The potential effects of surface roughness due to PICA ablation or tile gap filler material protrusions[21] were included by adding bump factors to the smooth-wall LAURA results.[6] Bump factors for turbulent shear stress ($\frac{\tau_{w,k}}{\tau_{w,0}}$) and heat flux ($\frac{q_{w,k}}{q_{w,0}}$) were taken from historical data in the form of curve fits as a function of the *roughness augmentation Reynolds number* (k^+):

$$\frac{\tau_{w,k}}{\tau_{w,0}} = 1 + 0.9\,(log_{10}k^+ - 1),\ 10 < k^+ < 70 \tag{3}$$

$$\frac{q_{w,k}}{q_{w,0}} = 1 + 0.6\left(\frac{\tau_{w,k}}{\tau_{w,0}} - 1\right) \tag{4}$$

where

$$k^+ = \frac{\rho_w U_\tau k_s}{\mu_w} \tag{5}$$

An equivalent roughness height ($k_s = k$) of 0.6 $\times 10^{-3}$ m was used for pre-flight analysis based on measurements of PICA test samples.[9] Using this assumed roughness height, Figure 8 shows the heat flux bump factors at MISP locations derived from LAURA smooth-wall turbulent solutions. The factors reach as high as 1.26 at locations T2 and T3, where the turbulence was already expected to augment heating the most. Lower bump factors were predicted near the nose (T5 and T7) and no augmentation was predicted in the stagnation region (T1 and T4), where turbulence was not expected to affect heating in the first place.

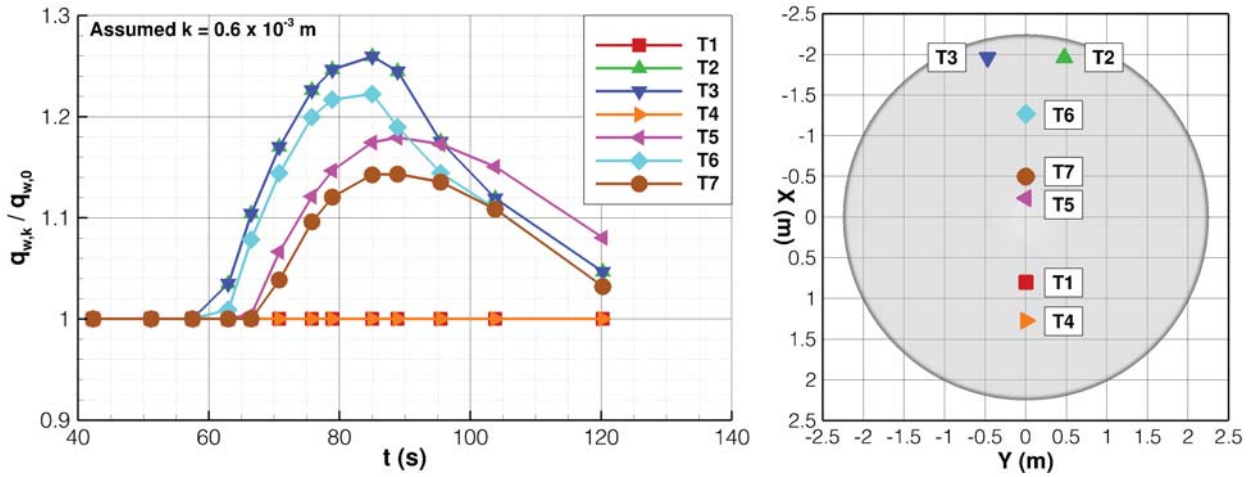

Figure 8. Turbulent Heating Bump Factors due to Distributed Roughness at MISP Locations for the Steep TPS Design Trajectory (Assumed $k = 0.6 \times 10^{-3}$ m)

Figure 9 shows results of pre-flight analysis at the TPS design trajectory's peak heating time. Laminar and Baldwin-Lomax turbulent heat flux without any design uncertainties are shown with the environments including all uncertainties used for TPS design. MISP locations T2 and T3 on the leeside were expected to experience the highest turbulent heat flux, whereas the MISP locations on the windside (T1 and T4) were not expected to see a turbulent heat flux that was any higher than the laminar level. The design leeside turbulent heat flux was approximately 58% higher than the smooth-wall turbulent heat flux from LAURA, mostly due to the potential effects of distributed surface roughness. Table 2 summarizes the peak TPS design conditions at critical heatshield and MISP locations. Although not shown in Figure 9, the T1 and T4 design heat fluxes included an uncertainty to account for the same unknown phenomenon that caused stagnation heating on wind tunnel models to exceed laminar CFD calculations.

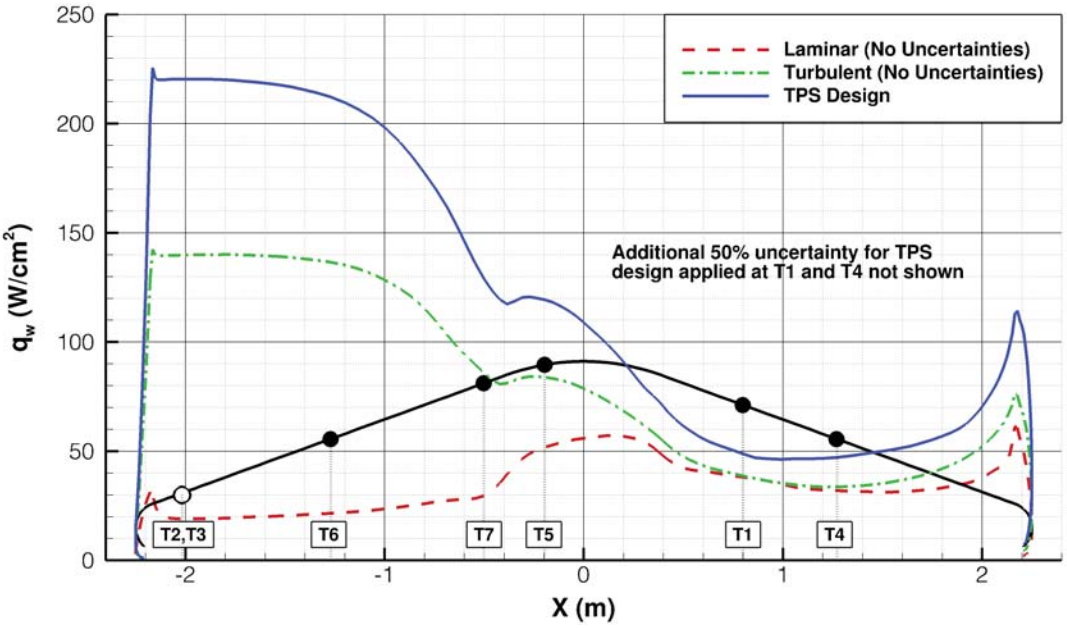

Figure 9. LAURA Laminar and Turbulent Heat Flux (Super-Catalytic) Compared to Design Heat Flux at Peak Heating for the TPS Design Trajectory

Table 2. Heatshield TPS Design Environments

Location	Peak q_w (W/cm^2)	Peak τ_w (Pa)	Peak p_w (atm)	Q_w (J/cm^2)
Leeside Flank (X = -1.795 m)	220	393	0.246	6104
Leeside Shoulder (Max. q_w)	226	465	0.242	6402
Leeside Shoulder (Max. τ_w)	203	490	0.208	5895
Stagnation Point (Max. p_w)	59	5	0.332	2605
Nose	119	127	0.239	4113
MISP T1	63	9	0.332	2662
MISP T2, T3	219	411	0.245	6112
MISP T4	57	8	0.331	2445
MISP T5	119	118	0.257	4167
MISP T6	212	304	0.244	5846
MISP T7	129	99	0.232	4236

III. BET CFD Results Compared to Pre-Flight Design

The BET was reconstructed[35−37] using MEADS data to estimate dynamic pressure, atmospheric density, and capsule attitudes. The reference time (t = 0) was chosen at a spacecraft clock time (SCLK) of 397501714.997338 seconds, or 540 seconds after the MEDLI power was turned on. Comparisons between the BET and design trajectories (steep and shallow) are shown in Table 3 and Figure 10. The BET's lower entry mass (m_i) and velocity (V_i) manifest themselves as reduced peak aerothermodynamic conditions compared to the steep design trajectory. The BET's dynamic pressure and turbulent heat flux are slightly lower than those of the steep design trajectory. The BET design turbulent heat flux was estimated using the *aerothermodynamic indicator* at the heatshield's maximum heat flux location,[7] which was developed via curve fits of the design environments:

$$q_{ind} = (1.99 \times 10^{-13})(\rho_\infty^{0.993})(V_\infty^{4.87}) \tag{6}$$

This heat flux indicator includes design uncertainties added to the LAURA smooth-wall turbulent heating.

Table 3. BET Compared to TPS Design Trajectories

Parameter	BET	TPS Design Steep/Shallow
Entry Mass, m_i (kg)	3152.5	3348
Atmosphere-Relative Entry Velocity, V_i (km/s)	5.85	5.90
Inertial Entry Flight Path Angle, γ_i (deg)	-16.12	-15.5/-14
Hypersonic Ballistic Coefficient, m/C_DA (kg/m^2)	137	145
Peak Dynamic Pressure, q_∞ (kPa)	15.91	16.15/12.85
Peak Design Turbulent Heat Flux Indicator, q_{ind} (W/cm^2)	214	226/185

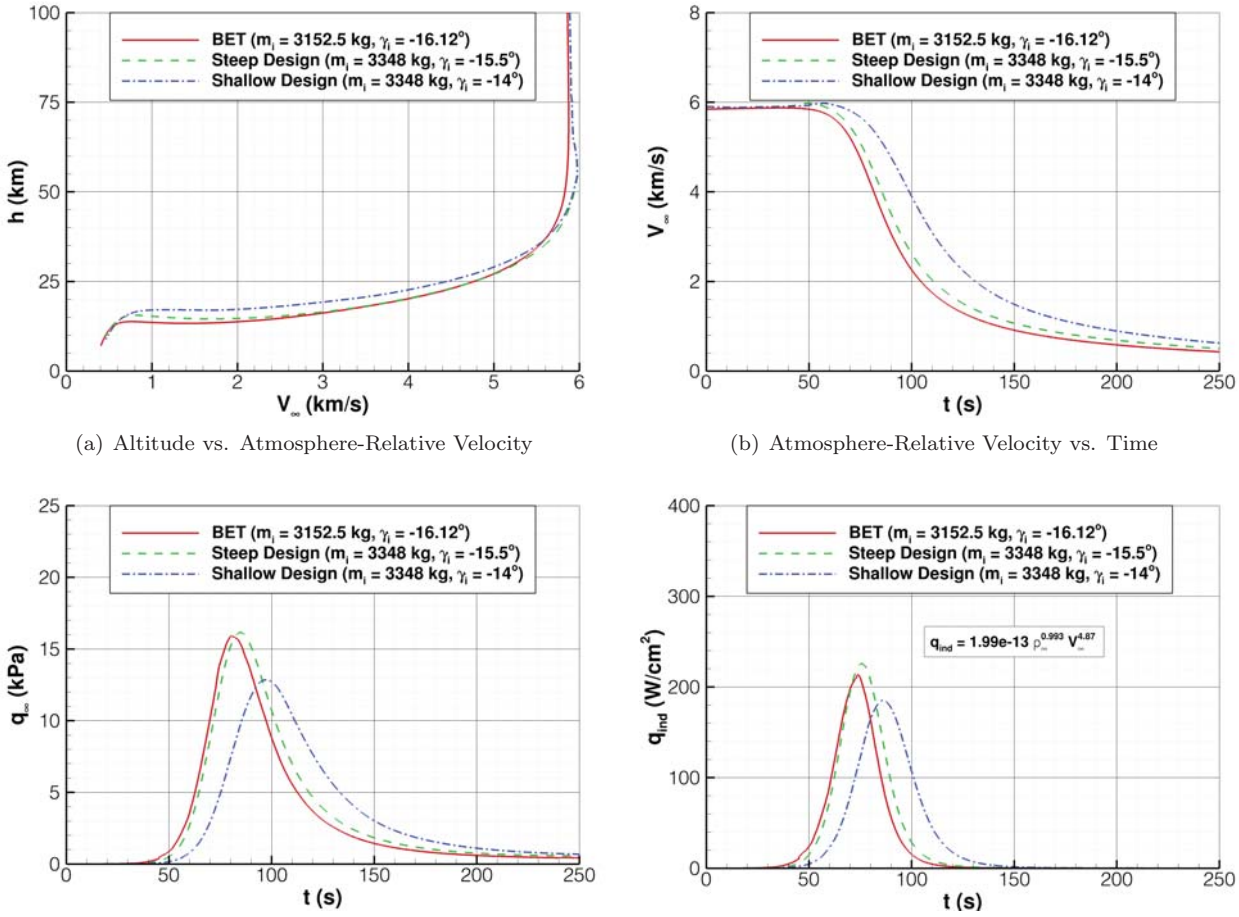

(a) Altitude vs. Atmosphere-Relative Velocity

(b) Atmosphere-Relative Velocity vs. Time

(c) Dynamic Pressure vs. Time

(d) Turbulent Heat Flux Indicator vs. Time

Figure 10. BET Compared to TPS Design Trajectories

LAURA solutions were obtained on the BET using the same modeling assumptions that were used to define the design environments: the Baldwin-Lomax algebraic turbulence model and a super-catalytic surface. DPLR Baldwin-Lomax results are also shown using a diffusion-limited surface catalysis model (fully-catalytic) that reduces the catalytic contribution to convective heating. Figure 11 and Table 4 summarize the conditions at the selected CFD points. The MEADS system measured a small angle of sideslip (< 1 degree),[36] so CFD solutions were obtained on a half-symmetry grid assuming no sideslip.

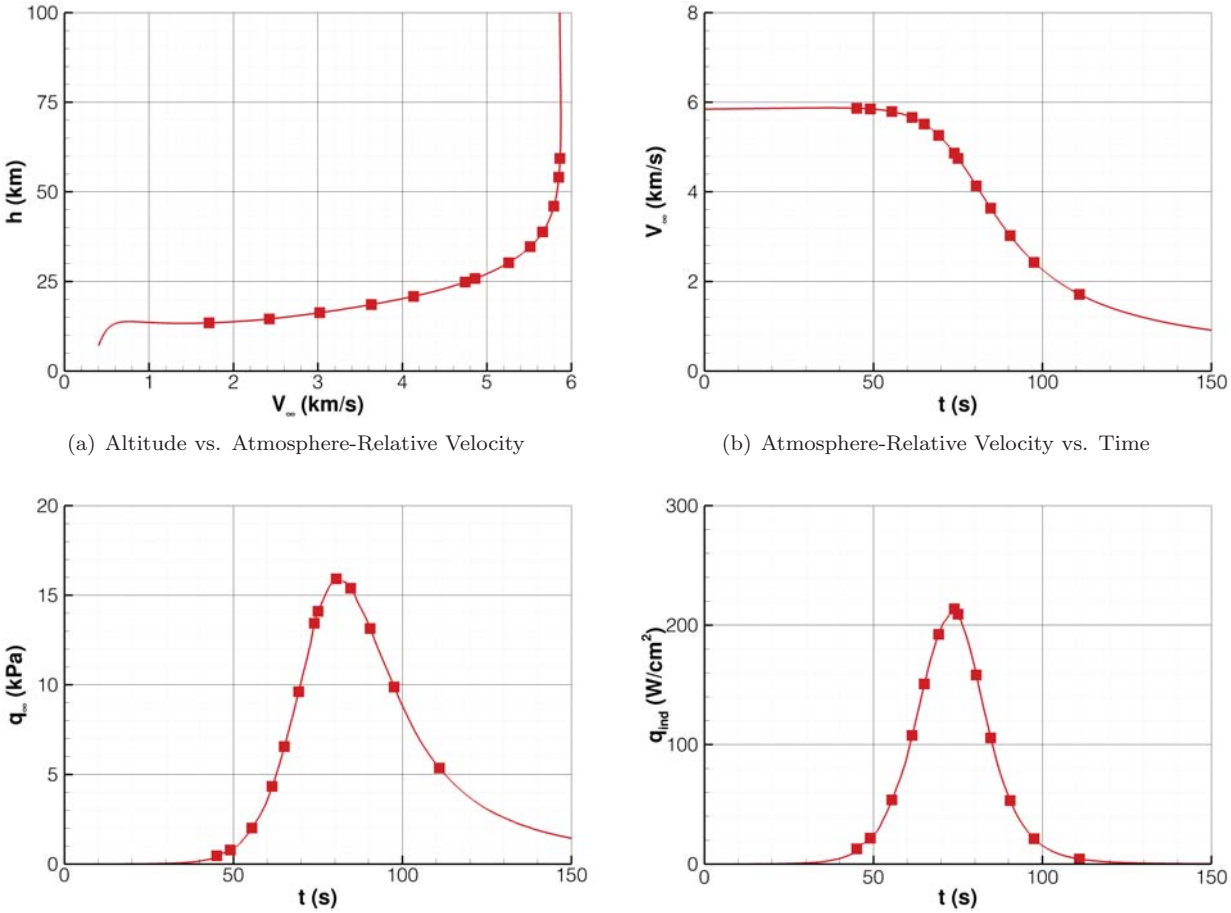

(a) Altitude vs. Atmosphere-Relative Velocity

(b) Atmosphere-Relative Velocity vs. Time

(c) Dynamic Pressure vs. Time

(d) Turbulent Design Heat Flux Indicator vs. Time

Figure 11. CFD Solution Points on the BET

Table 4. Freestream Conditions for CFD Solutions on the BET

t (s)	h (km)	V_∞ (km/s)	ρ_∞ (kg/m^3)	T_∞ (K)	q_∞ (kPa)	α (deg)	M_∞
45.1	59.3	5.866	0.265×10^{-4}	85.7	0.46	16.08	29.99
49.1	54.1	5.851	0.457×10^{-4}	127.0	0.78	14.79	30.00
55.5	46.0	5.793	0.120×10^{-3}	144.9	2.01	15.29	30.00
61.5	38.8	5.660	0.270×10^{-3}	157.0	4.33	15.66	28.44
65.1	34.7	5.515	0.431×10^{-3}	161.0	6.56	15.90	27.37
69.3	30.2	5.258	0.696×10^{-3}	168.5	9.62	16.20	25.51
74.0 (Peak q_w)	25.8	4.862	0.114×10^{-2}	169.8	13.43	16.10	23.50
75.1 (Peak τ_w)	24.8	4.745	0.125×10^{-2}	172.1	14.11	16.09	22.78
80.5 (Peak p_w)	20.8	4.133	0.186×10^{-2}	178.9	15.91	16.36	19.46
84.7	18.6	3.633	0.233×10^{-2}	182.7	15.39	16.59	16.93
90.5	16.3	3.023	0.287×10^{-2}	188.1	13.14	17.17	13.88
97.6	14.5	2.426	0.336×10^{-2}	192.2	9.88	17.47	11.02
111.0	13.4	1.713	0.365×10^{-2}	197.3	5.36	17.55	7.68

A comparison of the LAURA laminar Re_θ at peak heating on the BET and two design trajectories is shown in Figure 12. The BET Re_θ profile is very similar to the TPS results, and thus the conclusion remained that BLT would occur prior to BET peak heating on the heatshield leeside (MISP T2, T3, T6, and T7).

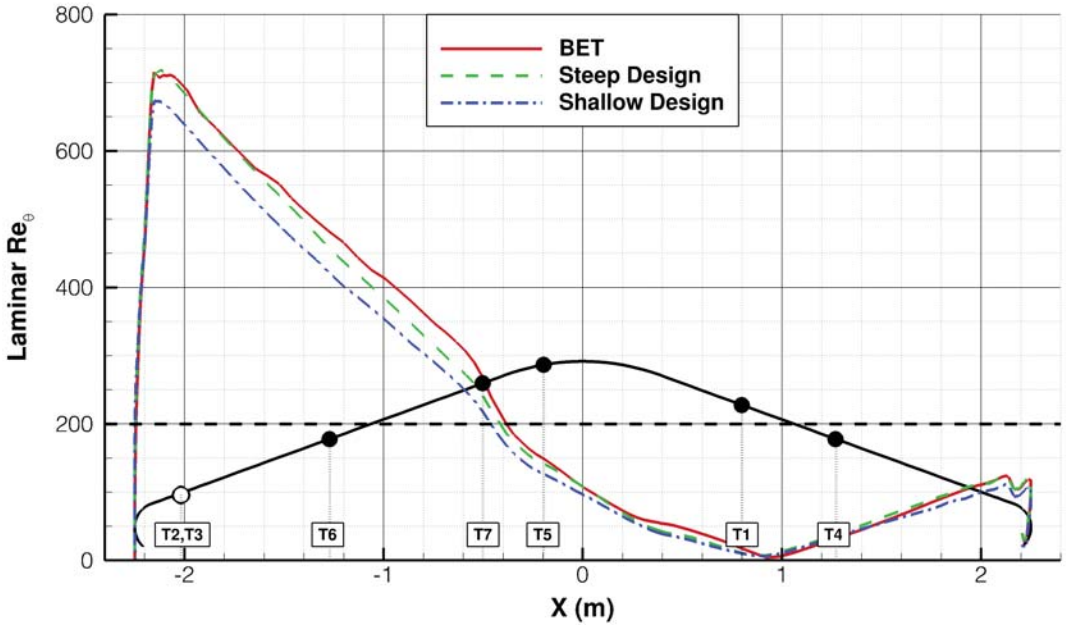

Figure 12. LAURA Laminar Re_θ at Peak Heating on the BET and TPS Design Trajectories

Figure 13 compares LAURA peak instantaneous conditions along the heatshield symmetry plane for the BET and TPS design trajectories. The BET peak heat flux, shear stress, and pressure lie in between the peaks for the steep and shallow design trajectories, which is consistent with the entry mass and velocity trends. The BET maximum heat flux on the leeside shoulder is about 6% lower than the maximum design value. The BET's total heat load is lower than it was for both design trajectories due to the shorter flight time and steeper entry flight path angle.

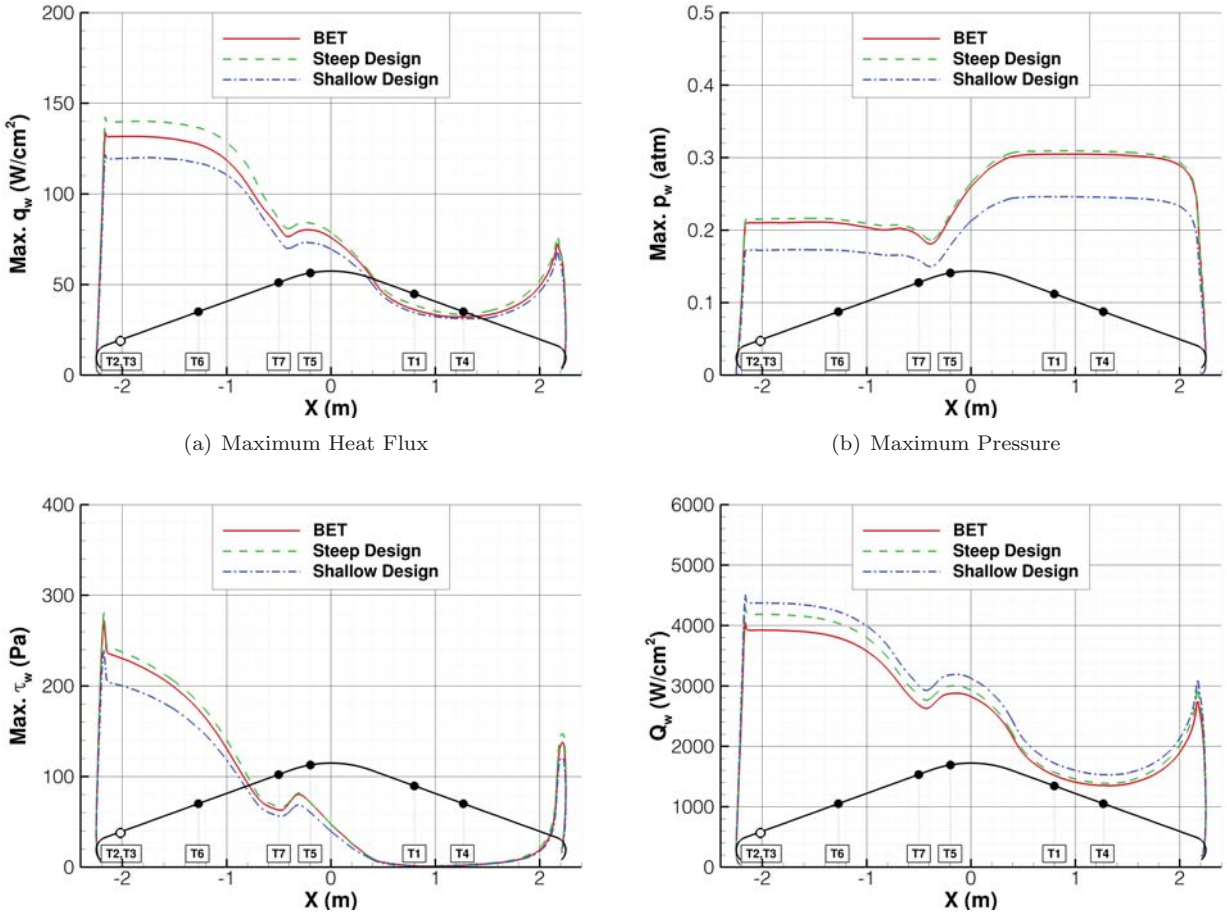

(a) Maximum Heat Flux

(b) Maximum Pressure

(c) Maximum Shear Stress

(d) Total Heat Load

Figure 13. LAURA Results on the BET Compared to Results on the TPS Design Trajectories (Baldwin-Lomax Turbulence Model, Super-Catalytic Wall, No Uncertainties)

The heatshield TPS design environments included the potential for distributed PICA surface roughness to augment turbulent heat flux above smooth-wall levels. The bump factor was applied to CFD smooth-wall heating results as a post-processing step. Figure 14 shows the MISP bump factors for the BET assuming a roughness height of 0.6×10^{-3} m. Given that the BET and TPS design trajectories are similar, the bump factors at each MISP location are approximately equal for the design and as-flown trajectories. If a uniform distributed roughness existed, locations T2 and T3 were expected to experience the highest increase in smooth-wall turbulent heating, by up to a factor of 1.25. Locations closer to the nose (T5 and T7) show lower bump factors and those in the stagnation region (T1 and T4) do not show any augmentation due to distributed roughness. Discrete roughness effects on turbulent heating were expected to only exist in the immediate vicinity of the heatshield tile gap fillers in the event that the gap filler protruded above the surrounding PICA. Pre-flight testing indicated that the filler material may recess more slowly than (or swell above) the surrounding PICA under low to moderate heating conditions.[9]

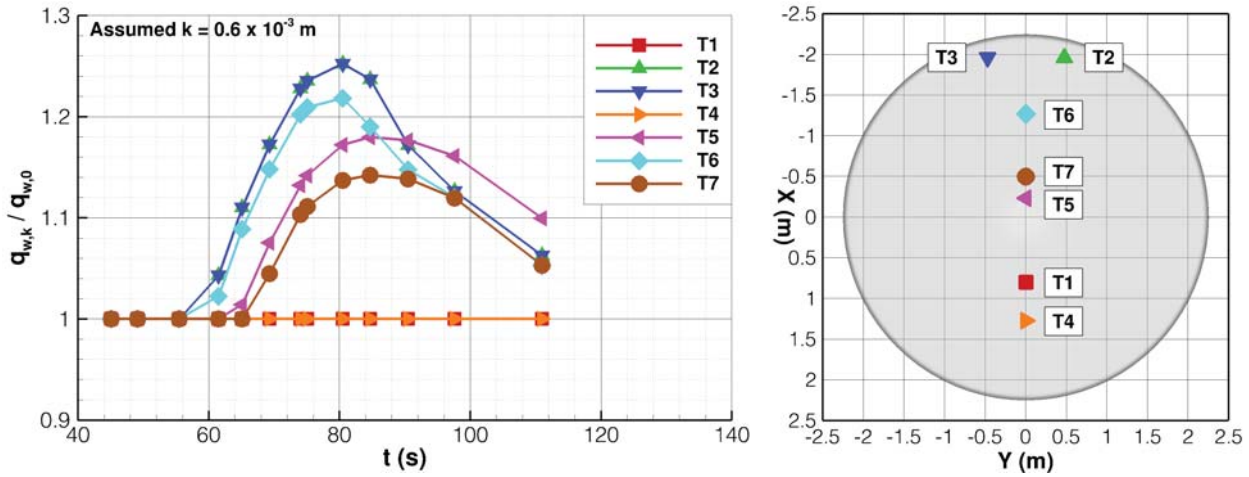

Figure 14. Turbulent Heat Flux Bump Factor Model due to Distributed Roughness at MISP Locations on the BET (Assumed $k = 0.6 \times 10^{-3}$ m)

IV. Reconstructed Heatshield Environments

The following sections discuss the MEDLI data products and reconstruction of the in-flight surface heating. Comparisons between the MEDLI data and the BET CFD results are used to explain various aspects of the heatshield aerothermodynamics: possible causes for the observed BLT timing, an assessment of roughness effects on turbulent heating, relative heating magnitudes at MISP locations, and an estimate of heating from shock layer radiation. Plausible explanations for discrepancies between the TPS design approach and reconstructed heating focus on surface roughness and radiative heating. All MEDLI data were acquired at a rate of 8 Hz during atmospheric entry.

A. Method of Heating Reconstruction

The Fully-Implicit Ablation and Thermal (FIAT) model was used to reconstruct surface heating from the MISP temperatures (inverse method).[29] This method is subject to uncertainties in the FIAT model, especially in the material properties and amount of PICA recession. The usual direct method also can be employed in which FIAT is used to calculate in-depth PICA temperatures using CFD-based heating. This method can be completed with different levels of CFD-based heating and the resulting in-depth temperatures can be compared to the MISP flight data to estimate the relative magnitude of actual surface heating. For instance, if the direct method results in FIAT in-depth temperatures that are higher than the MISP data, then the CFD heating that was fed into FIAT is likely higher than the actual heating experienced in flight. FIAT analysis is ongoing using both methods, including estimation of the uncertainty in reconstructed heat flux; the inverse results shown here represent the current state of the analysis.

CFD-based heating is not directly comparable to FIAT-based heating because the two methods solve different versions of the surface energy balance equation. The CFD analysis was decoupled from the FIAT analysis and does not account for the ablative material response. FIAT includes all energy terms: the incoming heating environment, the ablative material response, re-radiation, and conduction into the material. This surface energy balance[29] is shown in the following equation:

$$C_H(H_r - h_w) + \alpha_w q_{rad} + \dot{m}_g h_g + \dot{m}_c h_c - (\dot{m}_g + \dot{m}_c)h_w = \sigma\epsilon(T_w^4 - T_\infty^4) + q_{cond} \tag{7}$$

The first and second terms are the convective (q_w) and radiative heat fluxes. The remaining terms on the left-hand side represent the ablative material response. The terms $\dot{m}$ and h are mass flow rate and enthalpy, where the subscript g represents the pyrolysis gases (blowing) and the subscript c represents the char material (recession). The right-hand side represents re-radiation and conduction; the latter term is directly related to the measured in-depth temperatures. The decoupled CFD analysis only models the first term on each side of the equation, where T_∞ is set to 0. Radiative heating was not included in the design environments

because it was estimated to be small relative to convective heating. Estimates for the actual radiative heating component are included in this paper.

The FIAT analysis models the full surface energy balance with ablative material response, including the heating reduction due to pyrolysis gas blowing and char recession. FIAT solves the above equation iteratively with the CFD-based heating and an equilibrium surface chemistry model specifically designed for PICA. This process results in different wall enthalpies and temperatures between CFD and FIAT, and thus different heating values. The reported FIAT results include all terms on the left-hand side of the equation, which results in a lower heat flux than is reported from CFD. The main assumption in the FIAT analysis was that no recession occurred, which increases the apparent surface heating. The only conclusion from the MISP data is that recession was less than 0.1 inches since the shallowest thermocouples survived the entire heat pulse.

B. MEADS Data and Comparison to CFD Results

The only possible direct comparison between CFD and MEDLI data is via the MEADS pressures. A good comparison between CFD-based pressures and MEADS data is required, but not sufficient, for valid surface heating calculations. Table 5 and Figure 15 compare the MEADS pressure data to CFD results calculated on the BET. As expected, the CFD results compare very well to the data for the entire pressure pulse. The CFD results shown are laminar since the MEADS locations were expected to be laminar. Also, turbulence would not significantly affect surface pressures that are dictated by the inviscid flowfield. All sensors recorded pressure without any dropouts during EDL. Peak stagnation pressure (P1 and P2) occurred at about 80.7 seconds after atmospheric interface, or 0.2 seconds after the predicted time. The maximum pressures near the stagnation point were 0.302 atm (P1 and P3) to 0.303 atm (P2). The trend is for LAURA to under-predict pressures on the nose (P3, P4, and P5) and over-predict elsewhere on the heatshield (P1, P2, P6, and P7). The LAURA peak pressures are all within 2% of the measured peaks.

Table 5. LAURA Laminar Solutions on the BET Compared to MEADS Pressures

MEADS Location	MEADS Peak p_w (atm)	MEADS Time of Peak p_w (s)	LAURA at t=80.5 s Peak p_w (atm)	$100 \times \frac{p_{LAURA}-p_{MEADS}}{p_{MEADS}}$ (%)
P1	0.302	80.687	0.304	0.4
P2	0.303	80.699	0.305	0.7
P3	0.302	79.961	0.297	-1.9
P4	0.263	80.223	0.260	-1.4
P5	0.193	80.985	0.190	-1.9
P6	0.234	81.010	0.238	1.5
P7	0.237	80.248	0.238	0.1

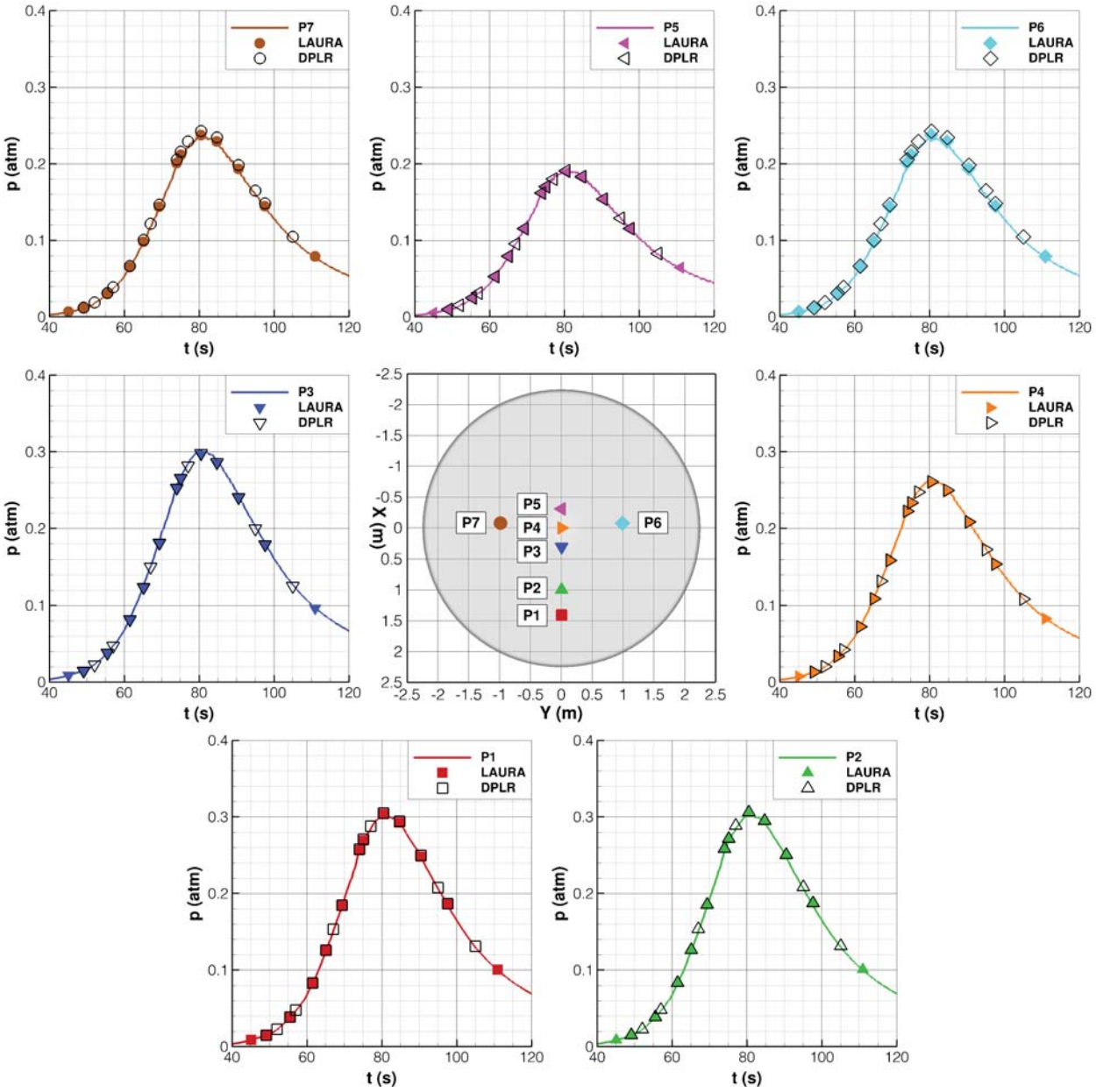

Figure 15. LAURA and DPLR Laminar Solutions on the BET Compared to MEADS Pressures

C. MISP Data and Boundary Layer Transition

The MISP sensors were arranged to detect BLT and to measure in-depth PICA temperatures that would allow for reconstruction of the surface heating. The MISP temperature data for the shallowest thermocouples (TCs at a depth 0.1 inches below the surface) are shown in Figure 16. As with the MEADS data, no MISP data dropouts occurred, indicating that the PICA did not recess beyond 0.1-*in*. Locations T2, T3, T6, and T7 all show a change in the temperature slope near 65 seconds; this slope discontinuity indicates BLT. The maximum temperature occurred at T7 (1049.14^oC at TC06), followed in descending order by T5, T2, T3, T6, T1, and T4. The location of instantaneous maximum heat flux does not necessarily correspond to maximum temperature. The maximum temperatures occurred at T7 and T5 because the laminar heat flux was highest at those locations prior to heatshield BLT.

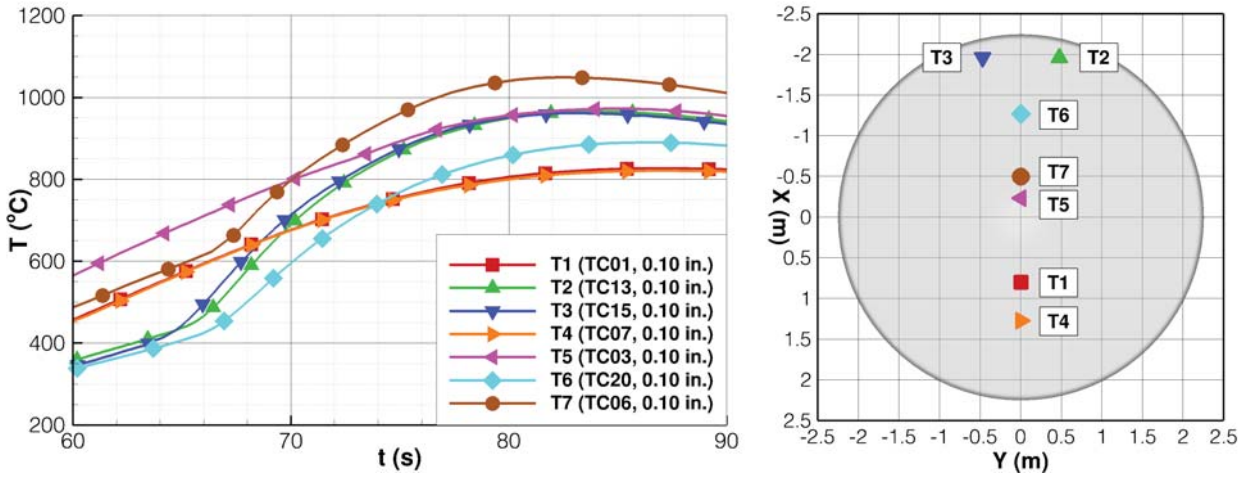

Figure 16. MISP Measured Temperatures at 0.1-*in* Depth. Transition Indicated by Slope Change for T2, T3, T6, T7, and Possibly T5.

The PICA design required that the temperature at the TPS/aeroshell bondine remained below 250^oC to maintain structural integrity. The deepest thermocouples at five MISP locations were located 0.7 inches below the surface and would experience higher temperatures than would the bondine at a larger depth. As shown in Figure 17, the maximum temperature at the 0.7-*in* depth occurred at T2 (132.22^oC), indicating that the bondine satisfied the TPS design requirement at all MISP locations.

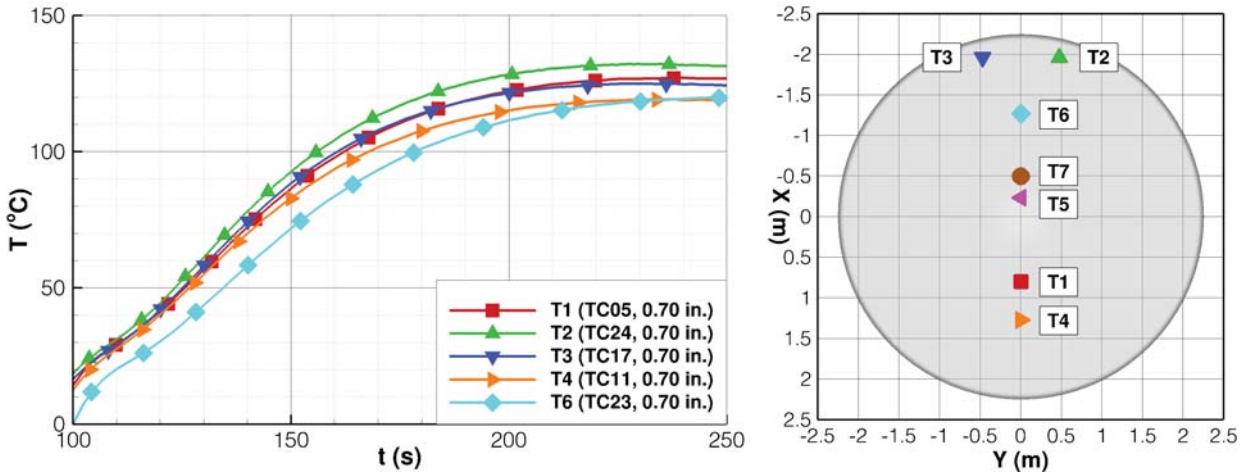

Figure 17. MISP Measured Temperatures at 0.7-*in* Depth. Maximum Temperatures Remained Below the TPS Bondline Allowable of 250^oC.

Figure 18 shows the time-derivative of temperature for the shallowest thermocouples (0.1-*in* depth). The sharp rise in the derivatives at locations T2, T3, T6, and T7 indicates BLT, which was expected for each location. The T5 curve has a small bump near 73 seconds that also may indicate BLT. If T5 experienced transition, it did so several seconds after T7 experienced BLT more than 10 inches downstream. Conversely, T1 and T4 remained laminar throughout the trajectory, as expected. All locations that experienced turbulent transition, except for T5, had onset times within about 2 seconds of each other (T3, T2, T7, and T6, in temporal order). Also, each of the turbulent locations transitioned from laminar to turbulent conditions over a span of about 3 seconds. The actual time of BLT is slightly earlier than the initial rise in the rate of temperature change because of the time lag between the transition event and the TC response 0.1 inches below the surface; this time lag is estimated to be about 2 seconds. Table 6 summarizes the temperature data at the shallowest thermocouples. The rate of temperature change (dT/dt) was highest at T2 and T3, where the highest turbulent heat flux was expected. The time of peak heating occurred before peak temperature,

as determined from FIAT inverse analysis.

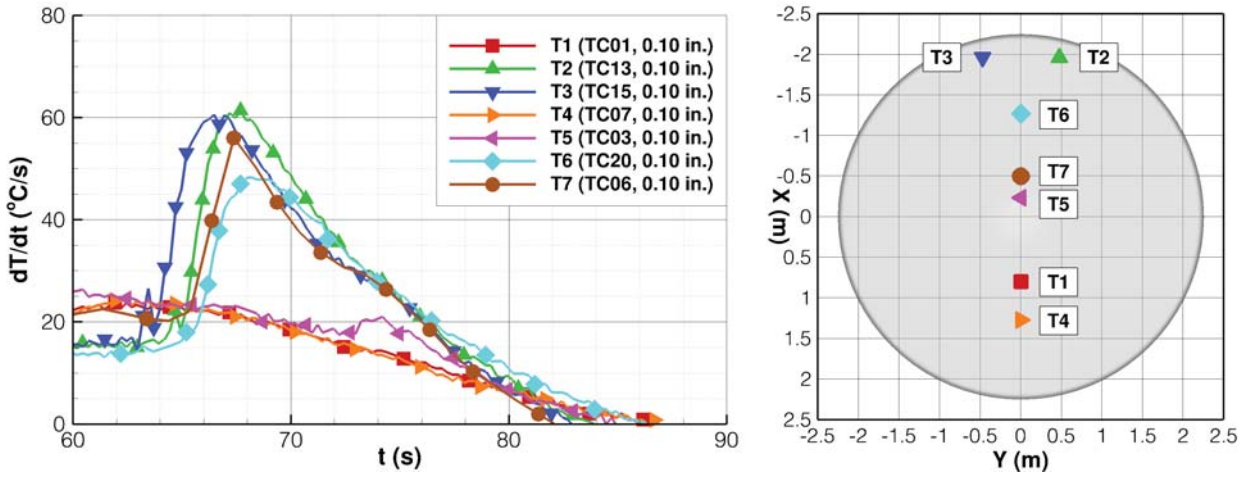

Figure 18. Time-Derivatives of MISP Measured Temperatures at 0.1-*in* Depth. Transition Indicated by Spikes for T2, T3, T6, T7, and Possibly T5.

Table 6. Summary of MISP Temperature Data at 0.1-*in* Depth

MISP Location	Transition Time $(s)^A$	Time at Peak q_w $(s)^B$	Peak T (^oC)	Time at Peak T (s)	Peak dT/dt $(^oC/s)$	Time at Peak dT/dt (s)
T1	N/A	74	826.48	86.932	23.72	61.932
T2	64	69	965.12	83.934	61.36	67.684
T3	63	68	961.42	82.958	60.61	66.458
T4	N/A	73	820.87	86.933	24.40	62.433
T5	73	75	972.52	84.956	26.76	58.706
T6	65	70	889.85	86.447	48.27	68.197
T7	65	74	1049.14	82.367	56.03	67.367

^{A}Based on initial rise in dT/dt

^{B}Based on inverse FIAT analysis of MISP temperatures[29]

D. MEADS Data and Boundary Layer Transition

An attempt was made to detect BLT via surface pressure measurements through the MEADS data, especially at locations P6 and P7 away from the symmetry plane ($Y = 0$). The difference in surface pressure between laminar and turbulent boundary layers was predicted to be much smaller than the uncertainty in CFD-based pressures. However, increased pressure oscillations may indicate the interaction of a turbulent boundary layer with the pressure port hole. Figure 19 shows MEADS pressures and the time-derivative of temperature at MISP T5. Also shown is the capsule's angle of attack oscillations during this time. The small bump in the T5 curve indicates possible BLT at about 73 seconds. The P5 pressure port is just downstream of T5, so turbulent conditions would have existed at P5 starting at 73 seconds. Figure 19 shows larger P5 pressure fluctuations starting at this time. Larger pressure fluctuations are also shown at P4, P6, and P7 after 75 seconds. The pressure oscillation magnitudes may be expected to follow the angle of attack oscillation magnitude, but the opposite is true in Figure 19. Fluctuations in angle of attack decrease as peak dynamic pressure is approached, at the same time the pressure noise at P4 through P7 increases. The pressures at P1 through P3 remain comparatively smooth, so the pressure oscillations at P4, P6, and P7 may indicate BLT rather than structural dynamics. If this is true, the transition events at P4, P6, and P7 may have been caused by upstream roughness from ablated PICA or gap filler material. Both P6 and P7 were located

approximately 3 inches downstream of the nearest PICA tile gap.

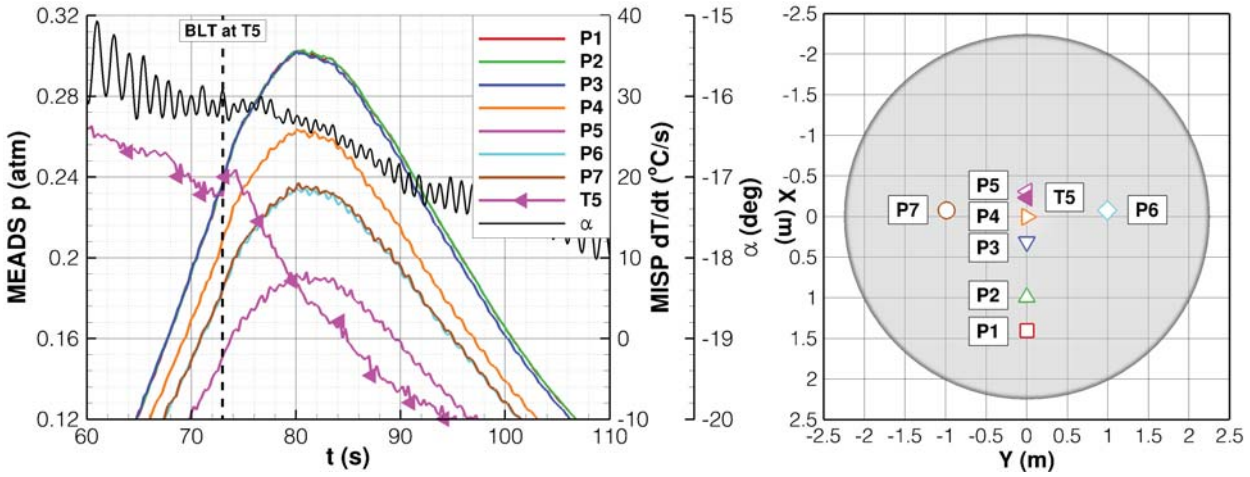

Figure 19. MEADS Pressures, Time-Derivative of MISP T5 Temperature at 0.1-*in* Depth, and Capsule Angle of Attack vs. Time

The pre-flight aerodynamics database was based on LAURA laminar predictions.[42] LAURA calculations using the Baldwin-Lomax model predicted that a fully-turbulent boundary layer would cause an increase in the angle of attack (α) of about 1 degree.[43] The source of the increase angle of attack was a higher turbulent shear stress contribution to the pitching moment coefficient. Figure 20 shows the time-derivative of temperature and reconstructed angle of attack. There is a coincident downward shift (increase in magnitude) in the angle-of-attack running average slightly after BLT begins at 63 seconds. This shift in angle of attack is smaller than 1 degree and may be the result of turbulent conditions on the heatshield leeside (near T2 and T3).

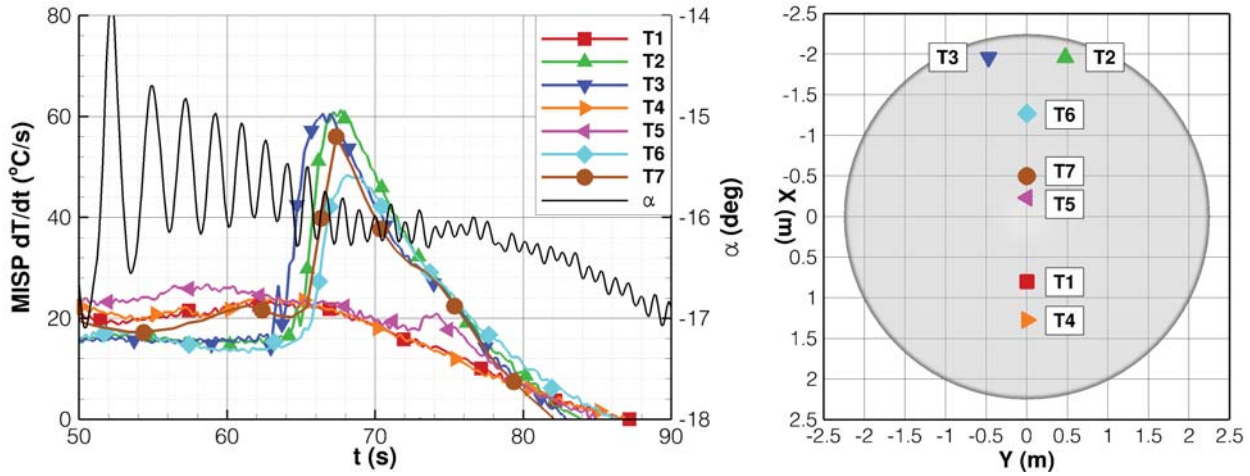

Figure 20. Time-Derivative of MISP Temperatures at 0.1-*in* Depth and Reconstructed Aeroshell Angle of Attack

E. Boundary Layer Transition and Roughness Effects

The design approach for heatshield BLT was to use a laminar $Re_\theta > 200$ criterion, which was exceeded prior to peak heating in all pre-flight trajectories. The LAURA laminar Re_θ results are shown in Figure 21 with the observed BLT times for 5 of the 7 MISP locations. The observed time of BLT, as indicated by the sharp rise in dT/dt, is summarized in Table 7. MISP locations T2, T3, and T6 all tripped to turbulent conditions after the time of calculated laminar $Re_\theta > 200$. MISP locations T7 and T5 tripped at a laminar $Re_\theta < 200$.

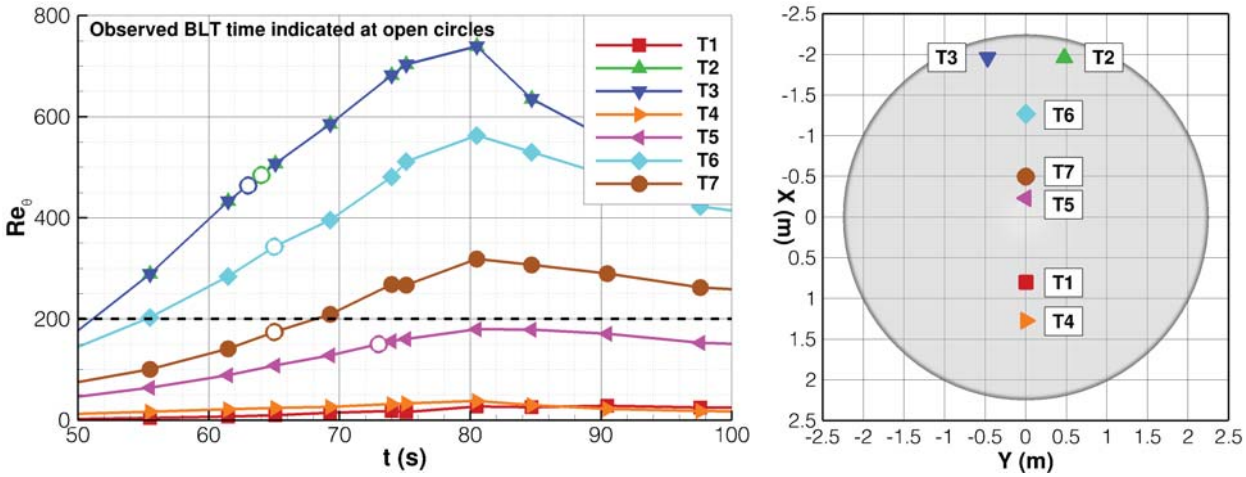

Figure 21. LAURA Laminar Re_θ at MISP Locations on the BET

Table 7. Boundary Layer Transition Compared to LAURA Laminar Re_θ on the BET

MISP Location	Transition Time $(s)^A$	Time at Peak q_w $(s)^B$	Time at LAURA $Re_\theta > 200$ (s)	LAURA Re_θ at Transition
T1	N/A	74	N/A	N/A
T2	64	69	51	484
T3	63	68	51	463
T4	N/A	73	N/A	N/A
T5	73	75	N/A	150
T6	65	70	55	342
T7	65	74	68	174

^{A}Based on initial rise in dT/dt

^{B}Based on inverse FIAT analysis of MISP temperatures[29]

The close spacing of the observed MISP transitions times indicate that roughness likely contributed to BLT. Figure 22 shows laminar boundary layer *roughness Reynolds number* ($Re_{k,k}$) values at each MISP locations using the same roughness height (0.6×10^{-3} m) that was used for the heat flux bump factor model. The $Re_{k,k}$ parameter is defined as:

$$Re_{k,k} = \frac{\rho_k u_k k}{\mu_k} \tag{8}$$

All turbulent MISP locations, with the exception of T5, had approximately the same $Re_{k,k}$ value at the time of BLT. The grouped $Re_{k,k}$ curves at the time of BLT indicates that roughness may have contributed, but the magnitudes are lower than what would be expected to cause BLT based on recent data; ballistic range testing on blunt models produced BLT from distributed roughness for $Re_{k,k}$ values between 150 and 300.[44] It is plausible that larger roughness elements from the PICA tile gap filler could have contributed to BLT at some of the turbulent MISP locations. However, no in-flight measurements of the in-flight PICA roughness were attempted. Figure 23 indicates that a roughness height closer to 2×10^{-3} m would have been needed to reach the conservative ballistic criterion ($Re_{k,k} > 150$).[44]

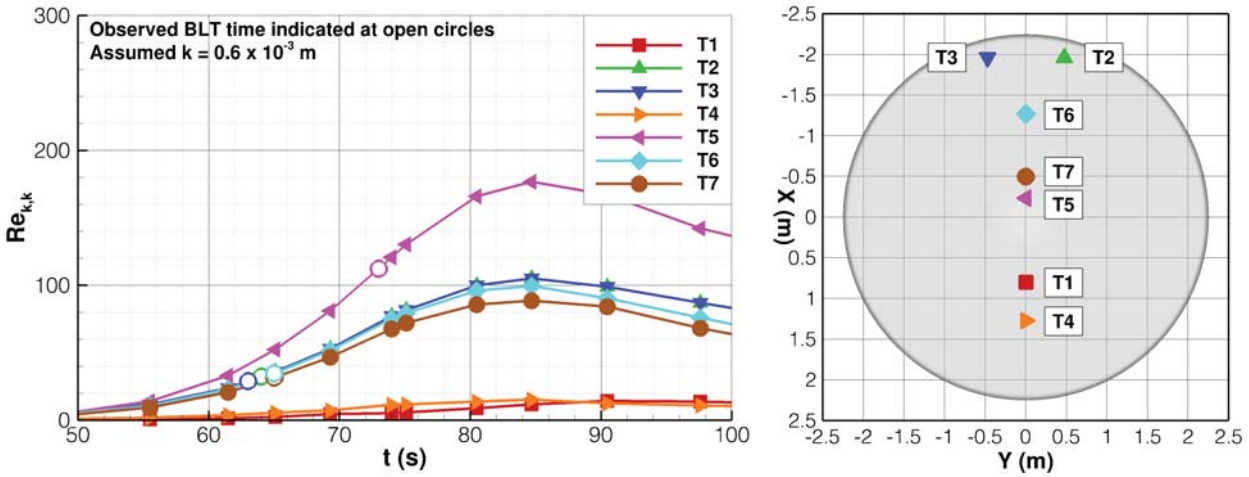

Figure 22. LAURA Laminar $Re_{k,k}$ at MISP Locations on the BET (Assumed k = 0.6 $\times 10^{-3}$ m)

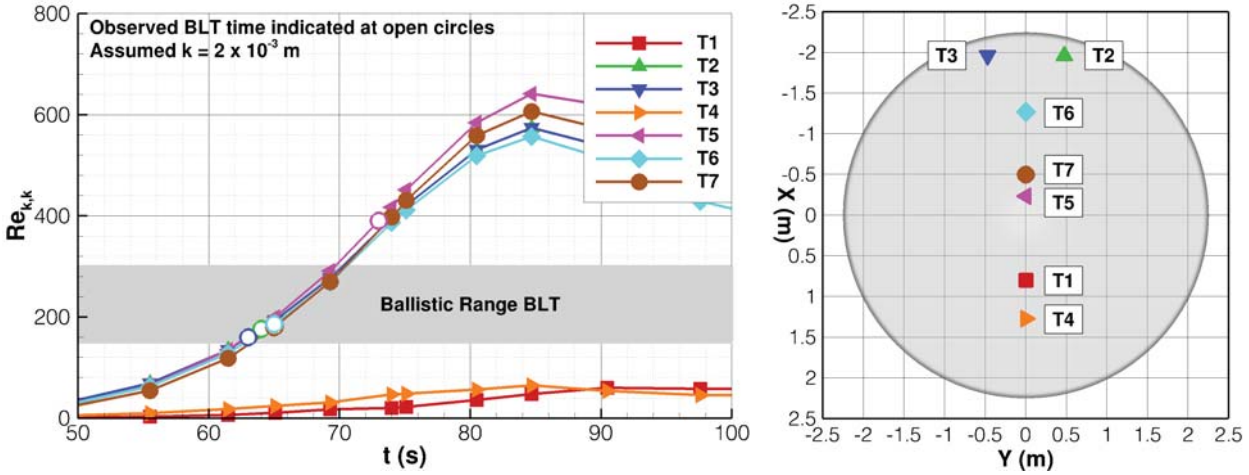

Figure 23. LAURA Laminar $Re_{k,k}$ at MISP Locations on the BET (Assumed k = 2 $\times 10^{-3}$ m) Compared to Ballistic Range Data[44]

F. CFD Results Compared to Reconstructed Heating

Figure 24 shows smooth-wall heat flux at each MISP location based on the LAURA (super-catalytic) and DPLR (fully-catalytic) solutions on the BET. The LAURA heating represents the upper bound on smooth-wall heating, not including the potential effects of surface roughness. The DPLR catalysis model reduces the convective heating below LAURA, especially at the leeside shoulder, where the reduction is about 25-30%. The DPLR model also predicted that the peak heating time would be several seconds earlier than LAURA's peak time. Locations T2 and T3 were expected to experience the highest turbulent heat flux, followed closely by T6. MISP T5 and T7 were expected to see about the same level of turbulent heating, assuming BLT occurred prior to peak heating. Laminar and turbulent CFD results resulted in approximately the same predicted heating at T1 and T4.

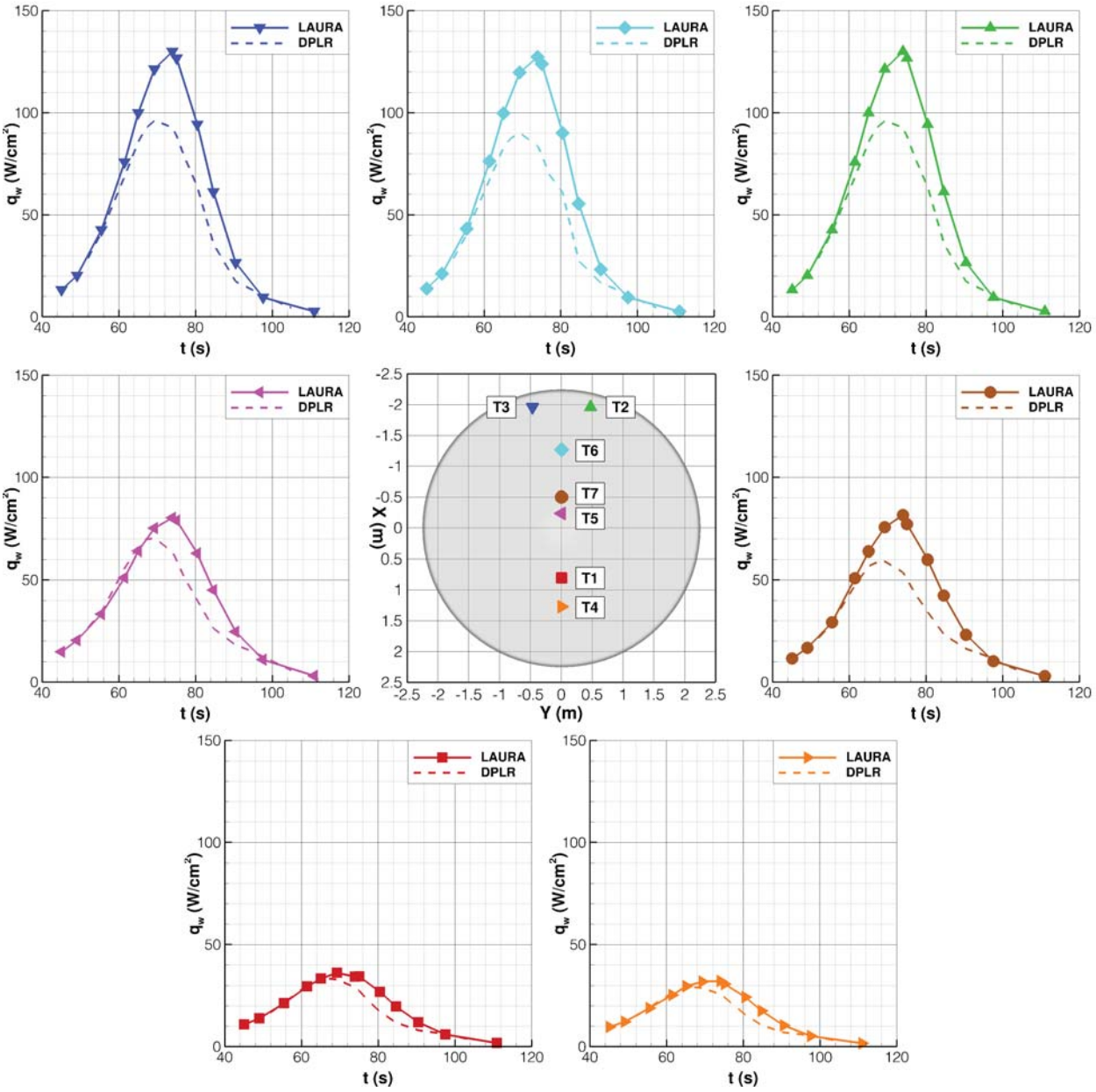

Figure 24. LAURA (Super-Catalytic) and DPLR (Fully-Catalytic) Smooth-Wall Turbulent Heat Flux at MISP Locations on the BET (No Uncertainties)

Direct analysis using the DPLR fully-catalytic heating was used to compare FIAT in-depth temperatures to the MISP data.[33] The FIAT temperatures at T2, T3, and T6 exceed the MISP temperatures, indicating that DPLR heating was higher than actual at those locations. However, the actual in-depth temperatures at T5 and T7 near the nose, and at T1 and T4 in the stagnation region, are all higher than FIAT predicts using DPLR fully-catalytic heating. This result indicates that the heating as predicted by DPLR was lower than the in-flight heating. Possible causes for this discrepancy include augmentation due to surface roughness and shock layer radiation, both of which are discussed below.

Figure 25 shows the results of the inverse FIAT analysis at each MISP location. The main assumption is that no recession occurred, which gives higher reconstructed surface heating. For the purposes of this paper, a +/-15% uncertainty is shown for the reconstructed heating due to unknown recession and uncertainty in PICA material properties. The effective heating shown in Figure 25 is not directly comparable to CFD heating because different terms are included in the surface energy balance. FIAT includes all contributors to surface heating, including ablation and pyrolysis. The CFD heating does not include the material response. The FIAT analysis indicates that, prior to BLT, T5 experienced the highest laminar heat flux; this was an expected result. The lowest laminar heating occurred at T2, T3, and T6, all on the heatshield leeside. Once BLT occurred shortly after 63 seconds, locations T2, T3, and T7 had the highest turbulent heating; T1 and T4 has the lowest heating during this time period. Pre-flight analysis predicted that T2 and T3 would experience the highest heating. Peak heating at T2 was slightly higher than it was at T3, possibly due to asymmetric BLT or a small angle of sideslip; the difference is within the estimated uncertainty of +/-15%. Location T7 experienced heating that was effectively equal to the heating at T2 and T3, if the FIAT uncertainty is included; this result was not expected based on the smooth-wall CFD results. Both T5 and T7 were located several inches downstream of the nearest PICA tile gap. Pre-flight testing showed that the gap filler could protrude above the surrounding PICA under certain conditions. However, CFD analysis predicted that the effects of gap filler on heating would be limited to a small region downstream of the gap.[21]

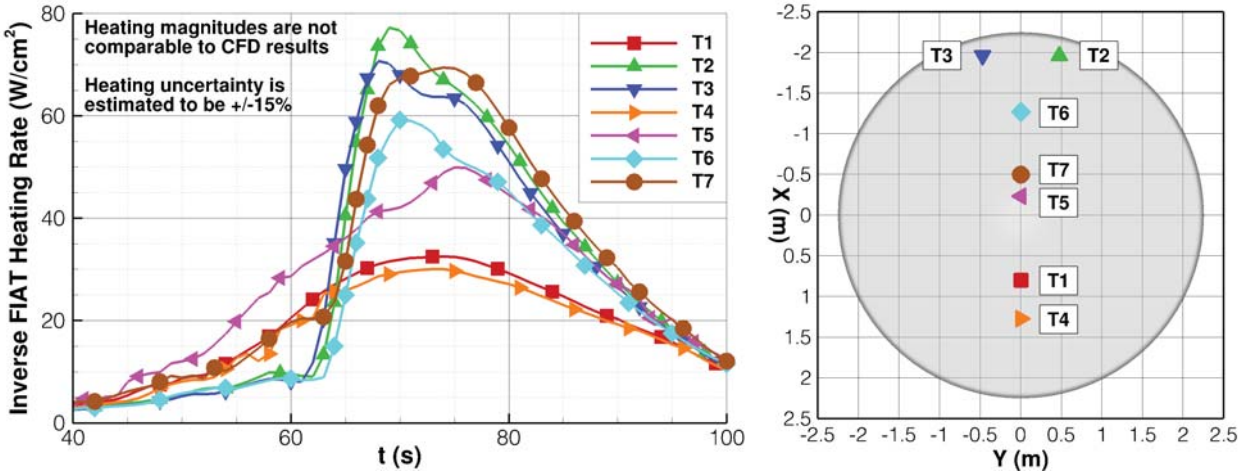

Figure 25. MISP Heating Rates Derived from FIAT Inverse Analysis

Figure 26 compares the CFD and FIAT results at each MISP location; the heating is non-dimensionalized by the peak value at T2 from the same analysis method. The CFD results are laminar prior to the observed BLT time and turbulent thereafter. The trends in non-dimensional heating can be used to understand the heating magnitudes in relation to the maximum turbulent heating at T2. Analysis is ongoing to understand the uncertainties in the FIAT results.[34] Under laminar conditions at T2, T3, and T6, the CFD heating qualitatively matches the FIAT results. After BLT occurred on the leeside flank, both CFD codes predicted that the T6 turbulent heating would reach nearly the level of T2 (0.94-0.96). However, the FIAT result at T6 shows a lower relative heat flux (0.77 of T2). The in-flight turbulent heating at T7 was significantly higher than either of the CFD codes predicted, in relation to the heating at T2. LAURA and DPLR predicted that peak smooth-wall turbulent heating at T7 would be about 0.62 of the peak heating at T2, whereas the FIAT-based T7 peak heating is about 0.90 of the T2 level. One possible explanation for the higher heating at T7 is surface roughness from an upstream location. The T5 sensor on the nose also saw higher relative

heating than the CFD predicted, but not to the extent seen at T7. The CFD codes and FIAT show that BLT occurred at T5 after the time of peak laminar heating; the time of peak turbulent heating occurred a few seconds later. In the stagnation region, T1 and T4 experienced higher peak heating in relation to T2 (0.42) than was predicted by CFD (0.27-0.32). This discrepancy could be the result of one or more effects, such as the heating bump observed in perfect gas wind tunnel data or shock layer radiation, the latter of which was not explicitly included in the pre-flight design environments due to the expected minimal effect.

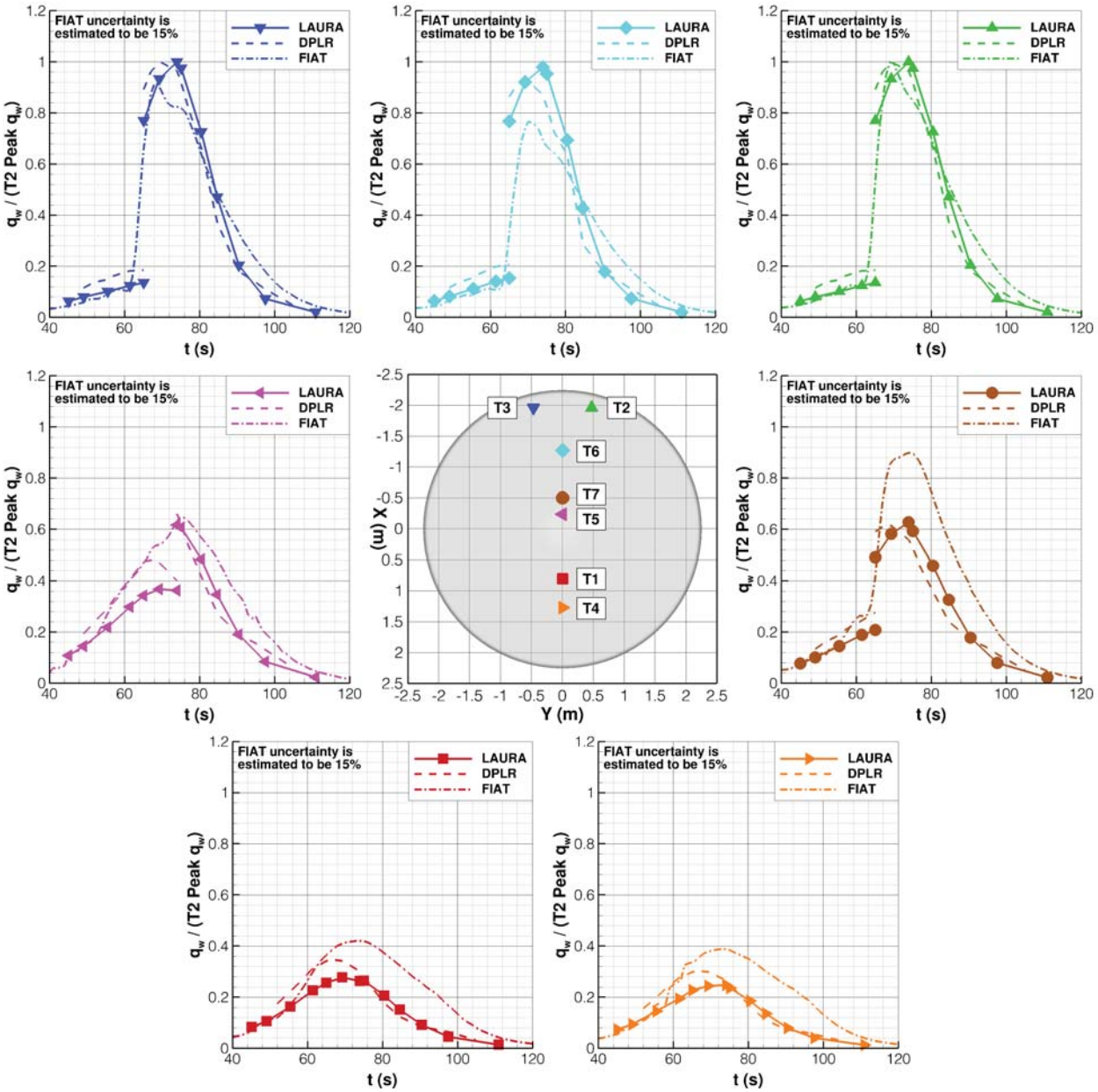

Figure 26. Normalized Heating Rate at MISP Locations: LAURA (Super-Catalytic Wall) and DPLR (Fully-Catalytic Wall) Smooth-Wall Results with Simulated BLT Compared to FIAT Inverse Analysis of MISP Data

Figure 27 shows the bump factor model added to the LAURA results at T7, assuming distributed roughness heights of 0.6×10^{-3} m and 2×10^{-3} m. The resulting increase in heating using the smaller roughness does not fully explain the under-predicted CFD smooth-wall heating, even if the estimated 15% FIAT uncertainty is included. The larger roughness brings the smooth-wall heating almost completely within the FIAT uncertainty. Thus, one or more of the following conclusions is true: the roughness height was larger than expected, the bump factor model under-predicts the heating augmentation, or the Baldwin-Lomax model under-predicts heating just downstream of the heatshield nose.

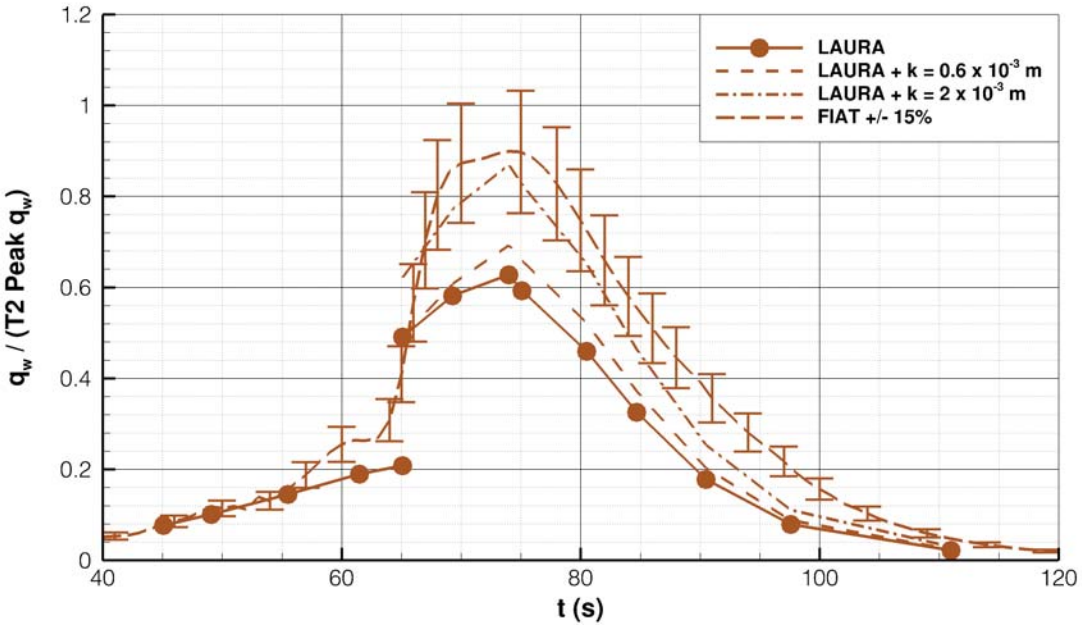

Figure 27. Normalized Heating Rate at MISP T7: LAURA Smooth-Wall Results and Bump Factor Model Compared to FIAT Inverse Analysis of MISP Data

Figure 28 shows CFD and FIAT results at various times in the heatshield pitch plane. The LAURA and DPLR results shown are laminar prior to BLT, with the exception of T5 at 69.3 seconds, and turbulent afterwards. In actuality, BLT does not occur immediately, either spatially or temporally. The CFD results at 69.3 seconds are turbulent, even though T5 had not yet completed BLT. The main reason for the quantitative differences between the non-dimensional CFD results is that DPLR predicted an earlier peak heating time for each MISP location compared to LAURA. Both LAURA and DPLR show non-dimensional heating that exceeds 1 on the leeside shoulder (negative X) because T2 and T3 were located away from the symmetry pitch plane where the heating was slightly lower. Prior to BLT at 55.5 seconds, the laminar CFD results and FIAT model predict similar qualitative non-dimensional heating. The FIAT analysis shows a lower relative heat flux at T6 on the leeside flank compared to the CFD results, even after BLT occurred. As was shown in Figure 26, T7 experienced a turbulent heat flux much closer to T2 than the CFD results indicate. At 74 seconds, the T7 reconstructed heat flux exceeds that of T2, even though the peak heat flux at T2 was higher. In the stagnation region, especially after BLT, T1 and T4 both experienced a higher relative heat flux than the CFD codes predicted. Again, this is possibly due to radiative heating not included in the CFD analysis.

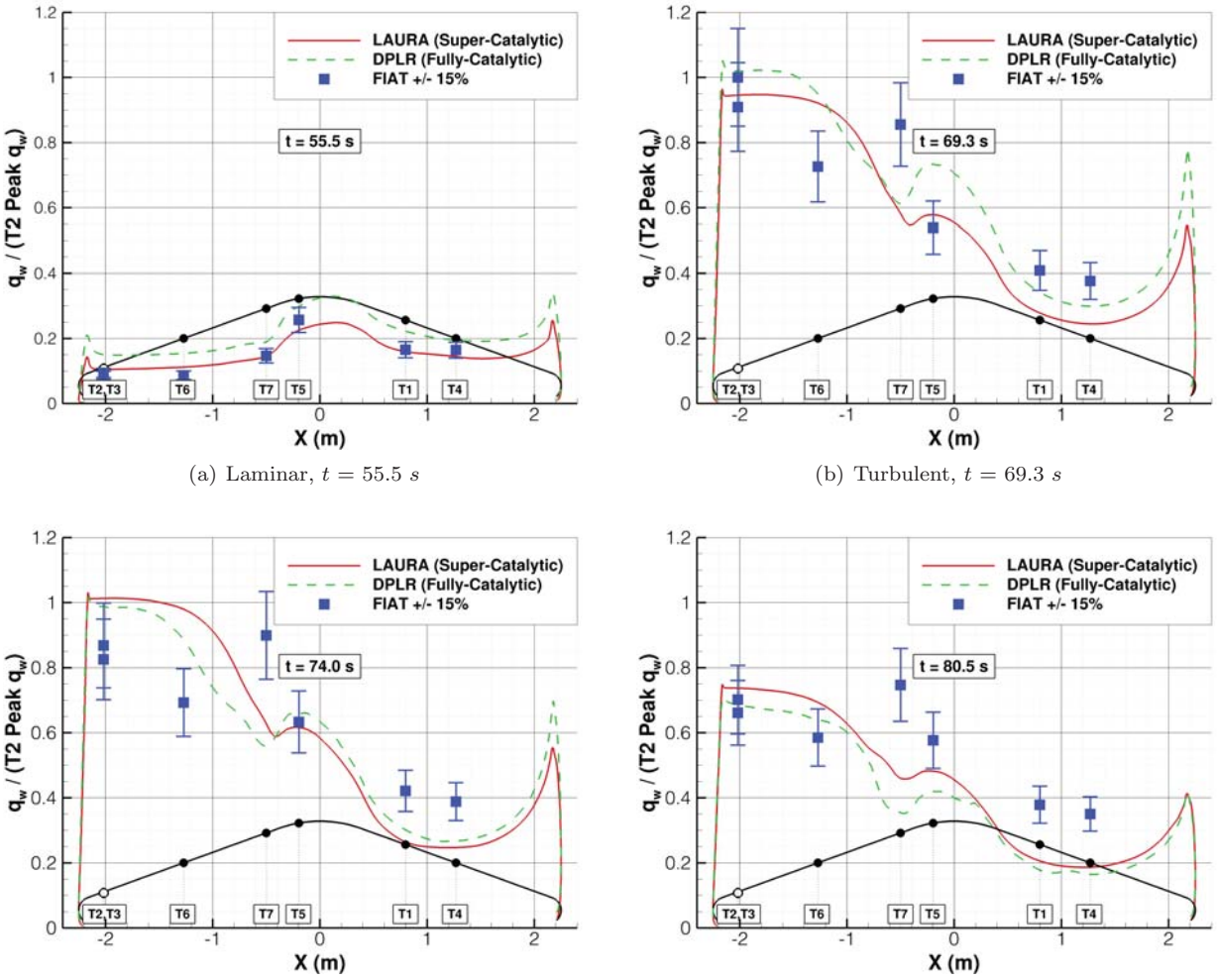

(a) Laminar, $t = 55.5$ s

(b) Turbulent, $t = 69.3$ s

(c) Turbulent, $t = 74.0$ s

(d) Turbulent, $t = 80.5$ s

Figure 28. Normalized Heating Rate in the Heathsield Pitch Plane: CFD Smooth-Wall Results Compared to FIAT Inverse Analysis of MISP Data

G. Shock Layer Radiation

MISP temperatures cannot be used to distinguish between convective and radiative heating. Radiative heating estimates were obtained from the Hypersonic Air Radiation Algorithm (HARA) code[45] using the BET conditions and LAURA flowfield. Figure 29 shows the LAURA convective heating at T7 with the HARA results, both of which are non-dimensionalized by the same quantity: the LAURA T2 peak convective heat flux. The CO and CO_2 infrared molecular bands are the dominant contributors to the radiative flux at MSL conditions.[46] Recent work[47−48] showed that HARA provides reasonable agreement with measurements at conditions relevant to the MSL cases. The same specie set that was modeled in LAURA was also included in HARA. The contribution from CN, which was excluded from the radiation calculations, is estimated to be negligible. The HARA results indicate that shock layer radiation reached a peak after convective heating, but the magnitudes do not fully explain the discrepancy between LAURA and inverse FIAT results.

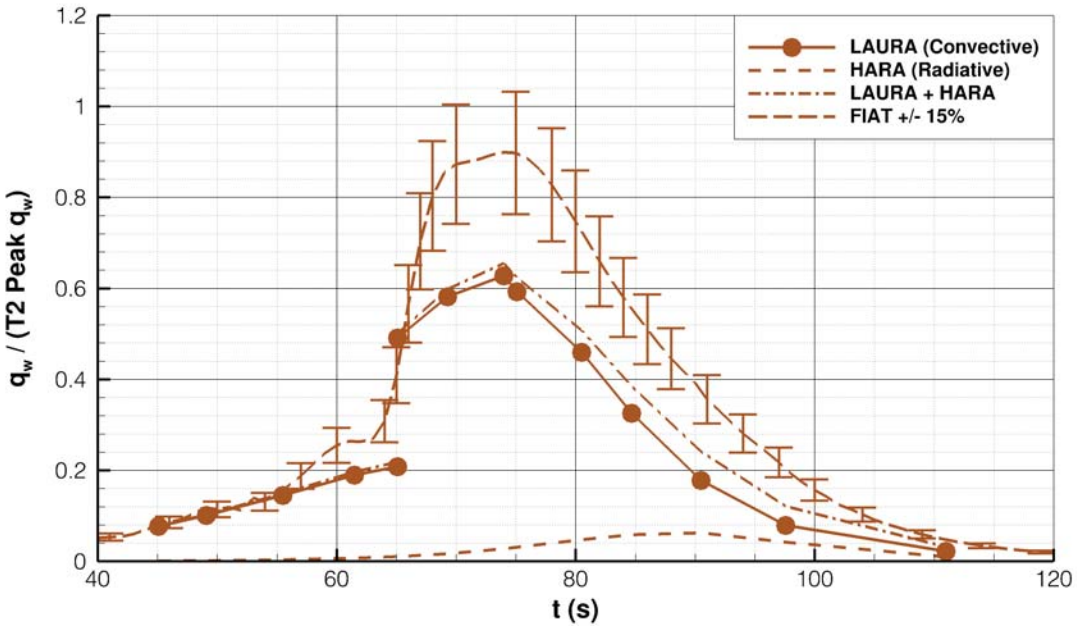

Figure 29. Normalized Heating Rate at MISP T7: LAURA (Convective) and HARA (Radiative) Compared to FIAT Inverse Analysis of MISP Data

Figure 30 shows LAURA and HARA results at T1 compared to the FIAT results. In the stagnation region, the radiative heating is a larger fraction of the total heating, as expected. HARA predicts that radiation constituted a significant portion of the total heating after peak convective heating; the two sources of heating are equal at about 90 seconds. However, the combined convective and radiative heating magnitude is still smaller than the reconstructed heating, even with the 15% FIAT uncertainty. Thus, the cause of the elevated stagnation heating remains unknown, but could be partially explained by radiation. It is unknown if the elevated heating at T1 and T4 is analogous to the bumps observed in perfect gas wind tunnel data.

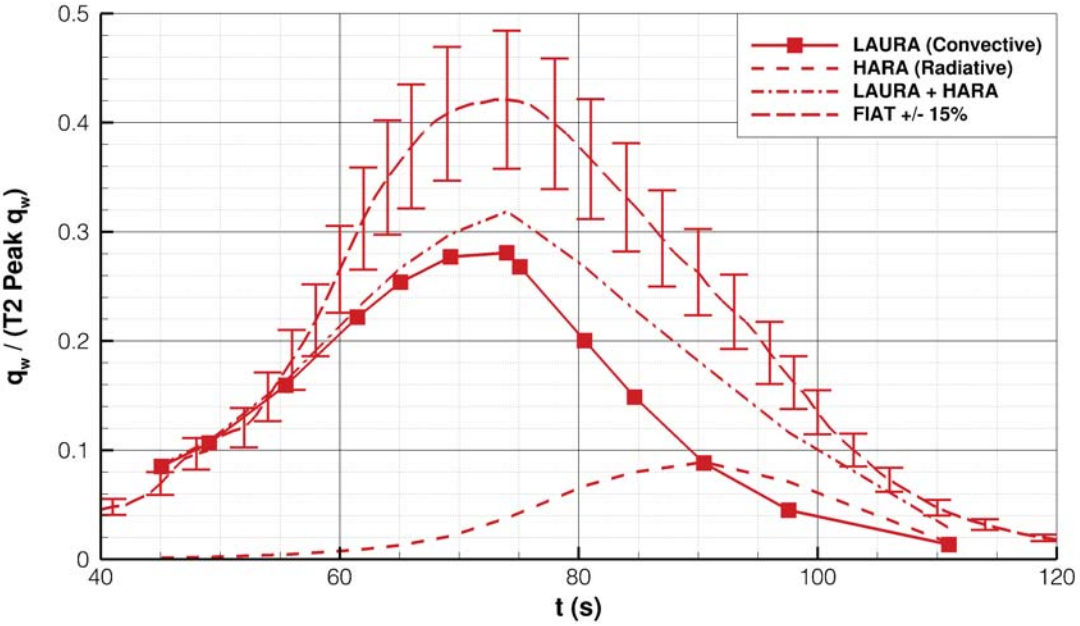

Figure 30. Normalized Heating Rate at MISP T1: LAURA (Convective) and HARA (Radiative) Compared to FIAT Inverse Analysis of MISP Data

V. Summary and Conclusions

The Mars Science Laboratory heatshield was designed to withstand turbulent conditions for the entire atmospheric entry trajectory. Pre-flight testing and analysis predicted that smooth-wall transition was highly likely and would only be exacerbated by roughness effects from the heatshield's ablative thermal protection system. The process used to define the design environments included the potential augmentation of turbulent heat flux from distributed surface roughness. In-flight measurements of heatshield temperatures confirmed that boundary layer transition occurred before peak heating at 5 of 7 measurement locations. Transition at 4 of the 5 turbulent locations occurred over a span of about 3 seconds, with the final turbulent location tripping about 8 seconds later. The exact cause of the transition events cannot be determined, but surface roughness likely played a role. However, the distributed roughness height needed to explain the observed transition time is larger than the roughness used in the pre-flight heatshield design. Transition may have also occurred at 2 or 3 other heatshield locations where pressure measurements show increasing oscillations.

Heatshield pressure data and reconstructed heating were compared to computational results on the as-flown entry trajectory. The calculated peak surface pressures at all 7 measurement locations were within 2% of the data. Inverse analysis with a material thermal response model was used to interpret the surface heating at 7 different locations, since direct heating measurements were not made. Reconstructed heating was non-dimensionalized by the maximum heat flux and compared to computational results. Prior to boundary layer transition, the highest laminar heating occurred near the heatshield's nose, as expected. Under laminar conditions, the leeside shoulder experienced the lowest heating, which was also expected.

After boundary layer transition occurred, the highest turbulent heating occurred at the predicted location near the heatshield's leeside shoulder. The stagnation region experienced the lowest heating, which also was expected. However, stagnation heating was a higher percentage of the maximum heating than was predicted; this could be partially due radiation that was not included in pre-flight calculations. However, post-flight radiation calculations do not fully explain the augmented stagnation heating. The main qualitative discrepancy between reconstructed turbulent heating and calculations was at a location just downstream of the heatshield nose. At this location, in-flight turbulent heating matched the maximum level at the shoulder within the uncertainty bounds; this was not predicted in pre-flight analysis. This augmented heating may have been the result of surface roughness. However, the heating bump factor model indicates that a roughness height larger than pre-flight measurements is needed to explain the observed augmentation.

The heatshield instrumentation confirmed that boundary layer transition occurred prior to MSL's peak heating time due to a combination of multiple sources: a large heatshield, an entry capsule with a high ballistic coefficient, a non-zero capsule angle of attack, and the potential effects of surface roughness from a tiled ablator thermal protection system. Future Mars heatshield's that share any of these characteristics will need to consider their effects in the aerothermodynamic design process. The use of a smooth-wall transition criterion may need to be augmented with roughness-induced transition analyses. However, the feasibility of characterizing heatshield roughness properties will need to be balanced against multiple constraints, including the resources needed to perform such analysis, the heatshield margins, and the risk tolerance of the mission.

Acknowledgments

The authors wish to thank Scott Berry at NASA Langley Research Center for discussions on boundary layer transition.

References

[1]Steltzner, A., et al, "Mars Science Laboratory Entry, Descent and Landing System Overview," AIAA Paper 2013-236, *AAS/AIAA Spaceflight Mechanics Meeting*, Kauai, Hawaii, 10 - 14 February 2013.

[2]Anonymous, "Entry Data Analysis for Viking Landers 1 and 2 Final Report," TN-3770218 (also NASA CR-159388), Martin Marietta Corp., November, 1976.

[3]Braun, R. D., Powell, R. W., Engelund, W. C., Gnoffo, P. A., Weilmuenster, K. J., and Mitcheltree, R. A., "Mars Pathfinder Six-Degree-of-Freedom Entry Analysis," *Journal of Spacecraft and Rockets*, Vol. 32, No. 6, November-December, 1995, pp. 670-676.

[4]Desai, P., Schoenenberger, M., and Cheatwood, F. M., "Mars Exploration Rover Six-Degree-of-Freedom Entry Trajectory Analysis," *Journal of Spacecraft and Rockets*, Vol. 43, No. 5, September-October, 2006, pp. 1019-1025.

[5]Desai, P. N., Prince, J. L., Queen, E. M., Cruz, J. R., and Grover, M. R., "Entry, Descent, and Landing Performance of the Mars Phoenix Lander," AIAA Paper 2008-7346, *AIAA Atmospheric Flight Mechanics Conference*, Honolulu, Hawaii, August, 2008.

[6]Edquist, K. T., Dyakonov, A. A., Wright, M. J., and Tang, C.-Y., Aerothermodynamic Design of the Mars Science Laboratory Heatshield, AIAA Paper 2009-4075, *AIAA Thermophysics Conference*, San Antonio, Texas, 22 - 25 June 2009.

[7]Edquist, K. T., Dyakonov, A. A., Wright, M. J., and Tang, C.-Y., "Mars Science Laboratory Entry Capsule Aerothermodynamics Environments: Revision B," JPL Document D-34661-B, 8 November 2010.

[8]Milos, F. S., Chen, Y.-K., Congdon, W. M., and Thornton, J. M., "Mars Pathfinder Entry Temperature Data, Aerothermal Heating, and Heatshield Material Response," *Journal of Spacecraft and Rockets*, Vol. 36, No. 3, May-June 1999.

[9]Beck, R. A. S., et al, "Development of the Mars Science Laboratory Heatshield Thermal Protection System," AIAA Paper 2009-4229, *AIAA Thermophysics Conference*, San Antonio, Texas, 22 - 25 June 2009.

[10]Driver, D. et al. "Arc Jet Testing in a Shear Environment for Mars Science Laboratory Thermal Protection System," AIAA Paper 2009-4230, *AIAA Thermophysics Conference*, San Antonio, Texas, June 2009.

[11]Tran, H., Johnson, C. E., Rasky, D. J., Hui, F. C., Hsu, M.-T., Chen, T., Chen, Y.-K., Paragas, D., and Kobayashi, L., "Phenolic Impregnated Carbon Ablators (PICA) as Thermal Protection Systems for Discovery Missions," NASA TM-110440, April 1997.

[12]Olynick, D., Chen, Y.-K, and Tauber, M. E., "Forebody TPS Sizing with Radiation and Ablation for the Stardust Sample Return Capsule," AIAA Paper 1997-2474, *AIAA Thermophysics Conference*, Atlanta, Georgia, June, 1997.

[13]Venkatapathy, R. and Reuther, J., "NASA Crew Exploration Vehicle Thermal Protection System, Lessons Learned," *International Planetary Probe Workshop*, Atlanta, Georgia, 26 June 2008.

[14]Gazarik, M., Wright, M., Little, A., Cheatwood, F. M., Herath, J., Munk, M., Novak, F., and Martinez, E., "Overview of the MEDLI Project," IEEE Paper 2008-1510, *IEEE Aerospace Conference*, Big Sky, Montana, March 2008.

[15]Edquist, K. T., Dyakonov, A. A., Wright, M. J., and Tang, C.-Y., "Aerothermodynamic Design of the Mars Science Laboratory Backshell and Parachute Cone," AIAA Paper 2009-4078, *AIAA Thermophysics Conference*, San Antonio, Texas, 22 - 25 June 2009.

[16]Edquist, K. T., Hollis, B. R., Dyakonov, A. A., Laub, B., Wright, M. J., Rivellini, T. P., Slimko, E. M., and Willcockson, W. H., "Mars Science Laboratory Entry Capsule Aerothermodynamics and Thermal Protection System," IEEEAC Paper 1423, *IEEE Aerospace Conference*, Big Sky, Montana, March 2007.

[17]Edquist, K. T., Dyakonov, A. A., Wright, M. J., and Tang, C.-Y., "Aerothermodynamic Environments Definition for the Mars Science Laboratory Entry Capsule," AIAA Paper 2007-1206, *AIAA Aerospace Sciences Meeting and Exhibit*, Reno, Nevada, January 2007.

[18]Edquist, K. T., Liechty, D. S., Hollis, B. R., Alter, S. J., and Loomis, M. P., "Aeroheating Environments for a Mars Smart Lander," *Journal of Spacecraft and Rockets*, Vol. 43, No. 2, March-April, 2006, pp. 330-339.

[19]Edquist, K. T., "Afterbody Heating Predictions for a Mars Science Laboratory Entry Vehicle," AIAA Paper 2005-4817, *AIAA Thermophysics Conference*, Toronto, Ontario, Canada, June 2005.

[20]Edquist, K. T., and Alter, S. J., "Computational Aeroheating Predictions for Mars Lander Configurations," AIAA Paper 2003-3639, *AIAA Thermophysics Conference*, Orlando, Florida, June 2003.

[21]Tang, C., Edquist, K. T., Wright, M. J., Sepka, S., and Cassel, A., "Numerical Simulations of Protruding Gapfillers on the Mars Science Laboratory Heatshield," AIAA Paper 2009-4077, *AIAA Thermophysics Conference*, San Antonio, Texas, June 2009.

[22]Hollis, B. R., and Collier, A. S., Turbulent Aeroheating Testing of Mars Science Laboratory Entry Vehicle, *Journal of Spacecraft and Rockets*, Vol. 45, No. 3, May-June 2008, pp. 417-427.

[23]Hollis, B. R., Liechty, D. S., Wright, M. J., Holden, M. S., Wadhams, T. P., MacLean, M., and Dyakonov, A., "Transition Onset and Turbulent Heating Measurements for the Mars Science Laboratory Entry Vehicle," AIAA Paper 2005-1437, *AIAA Aerospace Sciences Meeting and Exhibit*, Reno, Nevada, 11-15 January 2005.

[24]Wright, M. J., Olejniczak, J., Brown, J. L., Hornung, H. G., and Edquist, K. T.,"Modeling of Shock Tunnel Aeroheating Data on the Mars Science Laboratory Aeroshell," *Journal of Thermophysics and Heat Transfer*, Vol. 20, No. 4, October-December 2006, pp. 641-651.

[25]Hollis, B. R. and Prabhu, D. K., "Assessment of Laminar, Convective Aeroheating Prediction Uncertainties for Mars Entry Vehicles," *Journal of Spacecraft and Rockets*, Vol. 50, No. 1, January-February, 2013, pp. 56-68.

[26]Liechty, D. S. and Hollis, B. R., "Mars Science Laboratory Experimental Aerothermodynamics with Effects of Cavities and Control Surfaces," *Journal of Spacecraft and Rockets*, Vol. 43, No. 2, March-April 2006, pp. 340-353.

[27]Liechty, D. S. and Hollis, B. R., "Heat Shield Cavity Parametric Experimental Aeroheating for a Proposed Mars Smart Lander Aeroshell," AIAA Paper 2002-2746, *AIAA Fluid Dynamics Conference and Exhibit*, St. Louis, Missouri, June 2002.

[28]Little, A., et al, "The Mars Science Laboratory (MSL) Entry, Descent And Landing Instrumentation (MEDLI): Hardware Performance and Data Reconstruction," AAS Paper 13-078, *AAS Guidance and Navigation Conference*, Breckenridge, Colorado, 1 - 6 February 2013.

[29]Mahzari, M., Braun, R., White, T., and Bose, D., "Preliminary Analysis of the Mars Science Laboratory's Entry Aerothermodynamic Environment and Thermal Protection System Performance," AIAA Paper 2013-0185, *AIAA Aerospace Sciences Meeting*, Grapevine, Texas, 7 - 10 January 2013.

[30]Bose, D., White, T., Santos, J., Feldman, J., Mahzari, M., Olson, M., and Laub, B., "Initial Assessment of Mars Science Laboratory Heatshield Instrumentation and Flight Data," AIAA Paper 2013-908, *AIAA Aerospace Sciences Meeting*, Grapevine, Texas, 7 - 10 January 2013.

[31]Bose, D., White, T., Santos, J., Feldman, J., Mahzari, M., and Edquist, K., "A Reconstruction of Aerothermal Environment and Thermal Protection System Response of the Mars Science Laboratory Entry Vehicle," AAS Paper 13-311, *AAS/AIAA Spaceflight Mechanics Meeting*, Kauai, Hawaii, 10 - 14 February 2013.

[32]Bose, D., White, T., Feldman, J., Santos, J., and Mahzari, M., "Mars Science Laboratory Heat Shield Instrumentation and Post-Flight Analyses," AIAA Paper 2013-XXXX, *AIAA Thermophysics Conference*, San Diego, California, 24 - 27 June 2013.

[33]White, T., Mahzari, M., Bose, D., and Santos, J., "Post-flight Analysis of Mars Science Laboratory's Entry Aerothermal Environment and Thermal Protection System Response," AIAA Paper 2013-XXXX, *AIAA Thermophysics Conference*, San Diego, California, 24 - 27 June 2013.

[34]Mahzari, M., White, T., Braun, R., and Bose, D., "Inverse Estimation of Mars Science Laboratorys Entry Aerothermal Environment and Thermal Protection System Response," AIAA Paper 2013-XXXX, *AIAA Thermophysics Conference*, San Diego, California, 24 - 27 June 2013.

[35]Karlgaard, C., Kutty, P., Schoenenberger, M., Shidner, J., Munk, M., "Mars Entry Atmospheric Data System Trajectory Reconstruction Algorithms and Flight Results," AIAA Paper 2013-0028, *AIAA Aerospace Sciences Meeting*, Grapevine, Texas, 7 - 10 January 2013.

[36]Karlgaard, C., Schoenenberger, M., Kutty, P., Shidner, J., "Mars Science Laboratory Entry, Descent, and Landing Trajectory and Atmosphere Reconstruction," AAS Paper 13-307, *AAS/AIAA Spaceflight Mechanics Meeting*, Kauai, Hawaii, 10 - 14 February 2013.

[37]Schoenenberger, M., "Preliminary Trajectory Reconstruction Results of the Mars Science Laboratory Entry Vehicle," AAS Paper 13-306, *AAS/AIAA Spaceflight Mechanics Meeting*, Kauai, Hawaii, 10 - 14 February 2013.

[38]Cheatwood, F. M. and Gnoffo, P. A., "Users Manual for the Langley Aerothermodynamic Upwind Algorithm (LAURA)," NASA TM-4674, April 1996.

[39]Wright, M. J., Candler, G. V., and Bose, D., "Data-Parallel Line Relaxation Method for the Navier-Stokes Equations," *AIAA Journal*, Vol. 36, No. 9, 1998, pp. 1603-1609.

[40]Baldwin, B. and Lomax, H., "Thin Layer Approximation and Algebraic Model for Separated Turbulent Flows," AIAA Paper 1978-257, *AIAA Aerospace Sciences Meeting*, Huntsville, Alabama, January 1978.

[41]Menter, F. R., "Two Equation Eddy-Viscosity Turbulence Models for Engineering Applications," *AIAA Journal*, Vol. 32, No. 8, 1994, pp. 1598-1605.

[42]Schoenenberger, M., Dyakonov, A., Buning, Scallion, W., and Van Norman, J., "Aerodynamic Challenges for the Mars Science Laboratory Entry Descent and Landing," AIAA Paper 2009-3914, *AIAA Thermophysics Conference*, San Antonio, Texas, June 2009.

[43]Dyakonov, Schoenenberger, M., and Van Norman, J., "Hypersonic and Supersonic Static Aerodynamics of Mars Science Laboratory Entry Vehicle," AIAA Paper 2012-2999, *AIAA Thermophysics Conference*, New Orleans, Louisiana, 25 - 28 June 2012.

[44]Reda, D., Wilder, M. C., and Prabhu, D. K., "Transition Experiments on Large Bluntness Cones with Distributed Roughness in Hypersonic Flight," AIAA Paper 2012-0446, *AIAA Aerospace Sciences Meeting*, Nashville, Tennessee, 9 - 12 January 2012.

[45]Johnston, C. O., Brandis, A., and Sutton, K.,"Shock Layer Radiation Modeling and Uncertainty for Mars Entry," AIAA Paper 2012-2866, *AIAA Aerospace Sciences Meeting*, Grapevine, Texas, 7 - 10 January 2013.

[46]Lino da Silva, M., and Beck, J. "Contributions of CO2 IR Radiation to Martian Entries Radiative Wall Fluxes," AIAA Paper 2011-0135, Jan. 2011.

[47]Palmer, G. and Cruden, B. A., "Experimental Validation of CO2 Radiation Simulations", AIAA Paper 2012-3188, June 2012.

[48]Depraz, S., Perrin, M.-Y., Riviere, P., and Soufiani, A., "Infrared Emission Spectroscopy of CO2 at High Temperature. Part II: Experimental Results and Comparisons with Spectroscopic Databases," *Journal of Quantitative Spectroscopy and Radiative Transfer*, Vol. 113, 2012, pp. 14-25.